Spatio-temporal melt and basal channel evolution on Pine Island Glacier ice shelf from CryoSat-2.

Katie Lowery[1,2], Pierre Dutrieux[1], Paul R. Holland[1], Anna E. Hogg[2], Noel Gourmelen[3], and Benjamin J. Wallis[2]

[1]British Antarctic Survey, Cambridge, UK
[2]School of Earth and Environment, University of Leeds, Leeds, UK
[3]School of Geosciences, University of Edinburgh, Edinburgh, UK

Correspondence: Katie Lowery (katlow20@bas.ac.uk)

Abstract.

Ice shelves buttress the grounded ice sheet, restraining its flow into the ocean. Mass loss from these ice shelves occurs primarily through ocean-induced basal melting, with the highest melt rates occurring in regions that host basal channels — elongated, kilometre-wide zones of relatively thin ice. While some models suggest that basal channels could mitigate overall ice shelf melt rates, channels have also been linked to basal and surface crevassing, leaving their cumulative impact on ice-shelf stability uncertain. Due to their relatively small spatial scale and the limitations of previous satellite datasets, our understanding of how channelised ~~melting~~ melt evolves over time remains limited. In this study, we present a novel approach that uses CryoSat-2 radar altimetry data to calculate ice shelf basal melt rates, demonstrated here as a case study over Pine Island Glacier (PIG) ice shelf. Our method generates monthly Digital Elevation Models (DEMs) and melt maps with a 250 m spatial resolution. The data show that near the grounding line, basal melting preferentially melts a channel's western flank 50% more than its eastern flank. Additionally, we find that the main channelised geometries on PIG are inherited upstream of the grounding line and play a role in ~~forming~~ the formation of ice shelf pinning points. These observations highlight the importance of channels under ice shelves, emphasising the need to investigate them further and consider their impacts on observations and models that do not resolve them.

1 Introduction

Ice shelves, the floating extensions of ice sheets, surround the majority of the Antarctic coastline (Rignot et al., 2013) and act to buttress the grounded ice (Dupont and Alley, 2005; Goldberg et al., 2009; Gudmundsson, 2013). Between 1997 and 2021, Antarctic ice shelves lost a mass of 7,500 Gt (Davison et al., 2023), predominantly driven by basal melting induced by ocean forcing (Rignot et al., 2013; Davison et al., 2023). Notably, 90% of Antarctic mass loss since 1992 was concentrated in West Antarctica ~~(WA)~~ (Shepherd, 2018), where the rate of mass loss increased by 70% between 1994 and 2012 (Paolo et al., 2022). By 2017 ~~WA~~ West Antarctica had already contributed between 5.7 mm and 6.9 mm to global ~~sea level~~ sea-level rise (Shepherd et al., 2019; Rignot et al., 2019). The mass loss trend in ~~WA~~West Antarctica, and in particular the Amundsen Sea region, is thought to be driven by the intrusion of relatively warm Circumpolar Deep Water onto the continental shelf (Dutrieux et al.,

2014a; Jacobs et al., 1996; Shepherd et al., 2004). Further retreat, and potential collapse, of many ice shelves in the Amundsen Sea has been predicted (Joughin et al., 2010; Naughten et al., 2023; Joughin et al., 2014; Favier et al., 2014; Bett et al., 2024; De Rydt and Naughten, 2024).

Pine Island Glacier (PIG) in the Amundsen Sea has shown almost continuous acceleration (Joughin et al., 2003; Rignot et al., 2008; Mouginot et al., 2014) and thinning (Wingham et al., 2009) since the 1990s. By 2009, PIG's ice shelf flowed at 4 km/yr following a 75% acceleration since the 1970s (Mouginot et al., 2014). This acceleration was accompanied by a 50% increase in ice discharge at the grounding line (Medley et al., 2014). PIG's central grounding line also retreated by 31km (Rignot et al., 2014) between 1996 and 2011. During this retreat a pinning point, a localised area of grounded ice, formed in the centre of the ice shelf. Pinning points usually form on areas of anomalously high seabed topography. Pinning points significantly contribute to the buttressing capacity of an ice shelf (Favier et al., 2016; Schlegel et al., 2018) and have been shown to dictate the future of Thwaites Glacier (Bett et al., 2024). The pinning point in the centre of PIG ungrounded in 2011 and since then ~~its~~ an intially grounded thick column of ice has advected downstream, ephemerally regrounding (Rignot et al., 2014; Joughin et al., 2016). Following this, major calving events between 2017 and 2020 resulted in the ice front retreating ~~a further~~ 19 km and the ice shelf accelerating by 12% (Joughin et al., 2021).

On ice shelves, basal channels are elongated areas of relatively thin ice typically a few kilometres in width and spanning up to the whole length of the ice shelf. They have been observed on both Greenland and Antarctic ice shelves (e.g. Gourmelen et al., 2017; Dutrieux et al., 2013; Vaughan et al., 2012; Millgate et al., 2013; Drews et al., 2017; Alley et al., 2016; Motyka et al., 2011), including PIG ice shelf which has an abundance of basal channels (Dutrieux et al., 2013; Shean et al., 2019; Vaughan et al., 2012; Stanton et al., 2013). Channels modulate basal melt rates and, near the grounding line, focus the highest melt rates of an ice shelf within them (Dutrieux et al., 2013). Inside these channels, melt-induced buoyant freshwater plumes rise along the ice shelf base, entraining relatively warm water that enhances melting (Millgate et al., 2013; Gladish et al., 2012). However, further downstream, basal melt rates are ~~observed~~ thought to be higher on basal keels than within the channels (Dutrieux et al., 2013; Gladish et al., 2012). Channels can form from a variety of processes indicated by their inception location. Some form downstream of subglacial outflow locations (Le Brocq et al., 2013; Gourmelen et al., 2017; Marsh et al., 2016). Others form downstream of eskers on the seabed of grounded ice (Drews et al., 2017). Finally, a third type may be carved by buoyant ocean plumes resulting from instabilities of the coupled ice/ocean system (Alley et al., 2016; Sergienko, 2013). Gladish et al. (2012) and Millgate et al. (2013) showed that channels can reduce ice shelf area-integrated melt rates and also distribute melting more widely across an ice shelf, thus increasing the overall stability of an ice shelf. However, others have suggested channels can reduce the structural integrity of an ice shelf through increased surface and basal crevassing (Alley et al., 2016; Vaughan et al., 2012).

While ocean-driven basal melting stands as the primary contributor to mass loss in Antarctica, precise measurements of basal melt pose ongoing challenges. Various remote sensing techniques have been employed to derive melt rates (Shean et al., 2019; Zinck et al., 2023; Dutrieux et al., 2013; Paolo et al., 2022), alongside methods using sub-ice shelf oceanographic observations ~~(Davis et al., 2023; Dutrieux et al., 2014a; Schmidt et al., 2023)~~(Davis et al., 2023; Schmidt et al., 2023), ocean observations in front of ice shelves ~~(Jenkins et al., 2018)~~ (Jenkins et al., 2018; Dutrieux et al., 2014a) and direct in-situ observations of

melting using Automatic phase-sensitive Radio Echo Sounding ~~(ApRES; Nicholls et al., 2015; Davis et al., 2018; Vaňková et al., 2021)~~ (ApRES; Nicholls et al., 2015; Davis et al., 2018; Vaňková et al., 2021; Dutrieux et al., 2014b). Remote sensing techniques have given us a broad understanding of Antarctic-wide phenomena (Rignot et al., 2013; Adusumilli et al., 2020; Smith et al., 2020), but they have struggled to deliver melt rate fields with high spatial and temporal resolution. In-situ ApRES observations, on the other hand, have given us measurements with very high temporal resolution and accuracy but are constrained to a few point locations.

Remote sensing techniques are ever-improving, but there remains a trade-off between spatial and temporal resolution. Some ice shelf basal melt studies prioritise achieving high spatial resolution (<1 km) at the expense of temporal resolution (Dutrieux et al., 2013; Adusumilli et al., 2020; Zinck et al., 2023; Gourmelen et al., 2017), while others sacrifice spatial resolution to maintain adequate temporal resolution (Paolo et al., 2022). Due to these constraints, time-varying derivations of melting in basal channels are limited, leading to a lack of understanding of how channelised melting evolves and impacts ice-shelf stability. In this study, we introduce a novel methodology aimed at optimising both the spatial and temporal resolution of basal melt rates derived from surface elevation altimetry data. We apply this methodology to high-resolution CryoSat-2 Synthetic Aperture Radar Interferometer (SARIn) swath processed radar surface elevation measurements. This enables us to derive monthly Digital Elevation Models (DEMs) and basal melt maps at a spatial resolution of 250m. This study is completed as a case study over PIG; however, we note that this method can be applied to any ice shelf with sufficient surface elevation altimetry data where accurate velocity and divergence measurements exist. Leveraging this dataset, we explore the formation and growth of ice shelf basal channels, uncovering new insights into their evolution on PIG and their potential importance for the interaction and formation of ice shelf pinning points.

2 Data and Methods

2.1 CryoSat-2 Surface Elevation Data

We generate DEMs using CryoSat-2 (CS2) SARIn swath-processed radar altimetry data (Gourmelen et al., 2018). Over the Pine Island embayment area shown in Figure 1a, there are approximately 180 million elevation measurements between 2011 and 2023. These measurements are used to create monthly DEMs with a spatial resolution of 250 m. To achieve full coverage at this spatial resolution, each DEM requires a year's worth of data. We therefore produce a product with an annual resolution at monthly posting, as described below.

Before creating our DEMs many corrections are first applied to the CS2 observed ice shelf surface elevation data. Each CS2 elevation measurement has been corrected for tides, the inverse barometer effect (IBE) and firn air content. Tidal corrections have been applied from CATS model outputs (Howard et al., 2019) and IBE corrections have been taken from the CNES SSALLTO system provided by Meteo France. Firn air content has been taken from the Institute for Marine and Atmospheric research Utrecht (IMAU) firn densification model forced by RACMO model outputs (Veldhuijsen et al., 2023). We also note that the swath processing relies on the presence of an across-track surface slope to prevent left-right phase ambiguities. This can be challenging over some ice shelves. However, many studies have shown that we can retrieve swath elevation measurements for a

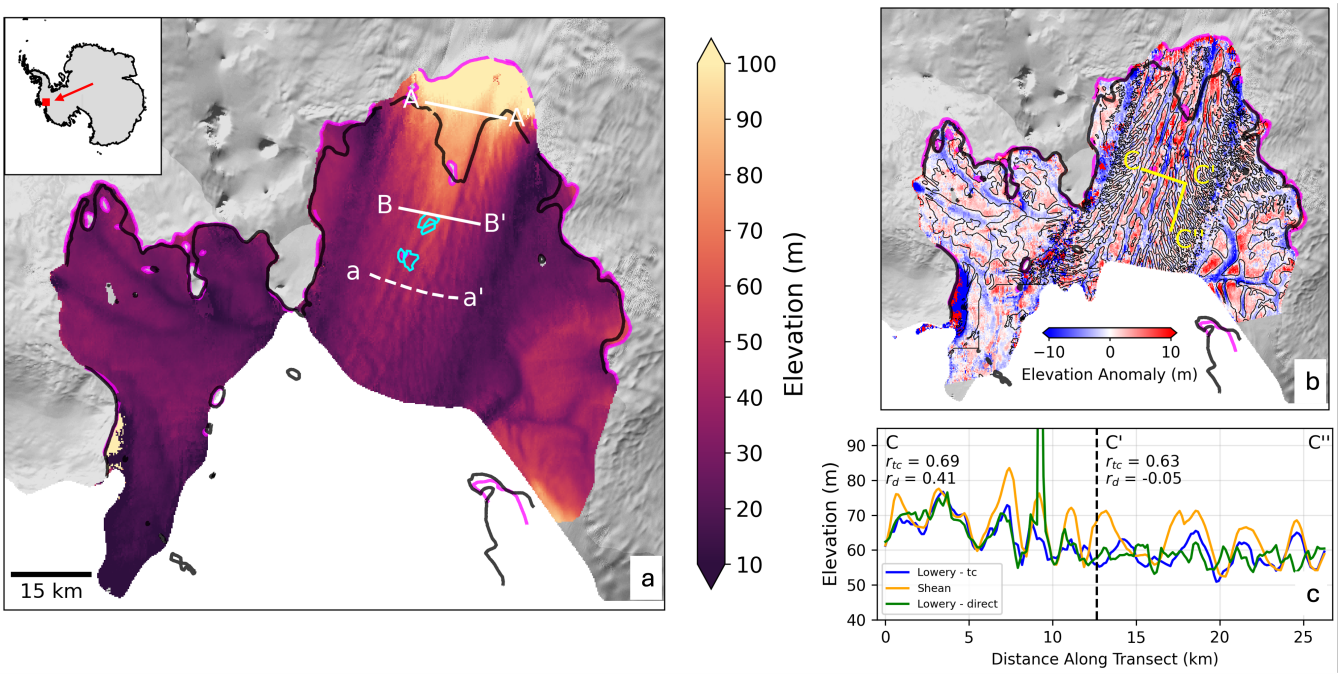

Figure 1. (a) A Digital Elevation Model (DEM) of Pine Island Glacier ~~in~~ from 2017 derived from CryoSat-2, with transects corresponding to sections used in Figure 7 and (c). ~~The~~ In (a) and (b) the 1996 and 2011 MEaSUREs grounding lines (Rignot et al., 2016) are shown in black and magenta, respectively. ~~The~~ (a) is also overlaid with areas of ephemeral re-grounding in 2017 as observed from Sentinel-1 using the ~~DROT~~ differential range offset tracking method (described in Section 2.3) ~~are shown~~ in ~~red~~cyan. The ~~white transects correspond to sections used~~ background in ~~Figure 7. Background:~~ (a) and (b) is a greyscale Landsat Image ~~Mosaic~~ Mosiac of Antarctica (LIMA) 15m. (b) shows a high-pass filtered CryoSat-2 DEM from December 2012. It is overlaid with the 0 m contour line from Shean et al. (2019) DEM in black. (c) Shows elevation profiles from our time-centered DEMs, our DEMs using the direct method and from the Shean et al. (2019) DEMs along the transect between C, C' and C'' shown in yellow on (b). The correlation of each of our methods with the Shean et al. (2019) DEM along the two sections of this transect are also shown.

significant portion of CS2 waveforms over many ice shelves (Gourmelen et al., 2017; Davison et al., 2023; Surawy-Stepney et al., 2023; W
. It is thought that the slight mis-pointing of CS2 prevents the complete cancelling of returns and therefore contributes to the coherence of data in these regions (Recchia et al., 2017). Once the corrections have been applied, any data of low quality have been removed. If the return has a coherence of less than 0.6, or its absolute difference with the Reference Elevation Model of Antarctica (REMA) is greater than 100 m, then the data have been removed.

The 12 months of data that ~~is required to created~~ are required to create a single DEM ~~is~~ are centred around the target date the DEM represents. The target date is the 1st of the month and all elevation data within 6 months of this date are gathered and advected to the location they would have been on the target date using ice velocity data. For example, if we were creating a DEM on July 1st, all observations acquired between January 1st and June 30th of the same year would be advected forward to

their location on July 1st and all observations between July 2nd and December 31st would be advected back to their location on July 1st. This process will be referred to as '~~time-centering~~time-centring' from here onwards. Specifically, if a given elevation measurement, h, is recorded in month m_0 with a location of (x_0, y_0) and the DEM being created is centred on month m_n, its time-centred location is given by:

$$(x_n, y_n) = (x_0 + \sum_{i=0}^{n-1} u_i dt, y_0 + \sum_{i=0}^{n-1} v_i dt), \quad (1)$$

where u_i and v_i are the velocities in the x and y directions evaluated at the (x, y) location of h at time step i and dt is the time step duration. Once this advection procedure has been applied to all measurements within 6 months of the target date, the resultant data points are gridded into 250 m x 250 m bins and that bin takes the median value of all its members. Advection is calculated using ITS_LIVE annual velocity mosaics (Figure 2b) and with a monthly time step. With CS2 surface elevation data spanning January 2011 to December 2023, our monthly DEMs start from July 2011 and extend to July 2023.

We have chosen to implement this ~~time-centering~~ time-centring method because it more accurately represents the surface of the ice shelf when combining a year of data than by directly binning the observations (Figure 1c and Figure A1). Temporal averaging is required to obtain 250 m horizontal resolution but, over a year of coverage, a parcel of ice could have crossed 16 of the 250 m grid boxes (assuming a velocity of 4 km/yr). By simply binning these observations, ice shelf surface geometries will be smoothed over a few kilometres, removing our ability to observe changes within channels and any features that are not exactly aligned with ice flow. By adopting the ~~time-centering~~ time-centring process, we reduce the aliasing of these features (Figure ~~A1).~~ 1c). Along the main trunk of the ice shelf the distribution of surface troughs and ridges (associated with basal channels and keels) in our time-centered DEMs show good agreement with a higher-resolution, but less frequently acquired, WorldView-derived DEM from Shean et al. (2019) (Figure 1b). While our CryoSat-2 DEMs successfully capture the primary longitudinal channel features, they do not resolve small transverse channels as clearly. However, the time-centring method captures these surface features with substantially greater accuracy than the direct method (Figure 1c). Between C' and C" of the transect shown in Figure 1b, the correlation with the Shean et al. (2019) DEM improves from –0.05 using the direct method to 0.63 with the time-centring approach.

~~To create the DEM, we advect elevation measurements to their predicted positions at~~ Despite the overall consistency in feature distribution, our CryoSat-2 DEMs underestimate the amplitude of channels relative to the Shean et al. (2019) product (Figure 1c). This underestimation occurs primarily through an underestimation of the surface ridges. While there are a number of reasons for this bias (firn penetration, averaging in time etc), we assume that it is consistent in time and therefore does not impact the temporal change observed throughout this paper.

The DEMs are generated by advecting elevation data to their estimated positions on the target date, ~~ignoring any thickness changes during the advection~~ while neglecting changes in ice thickness during this process. Although this assumption introduces some uncertainty, its impact on the final DEM is minimised because the advection is performed both forward and backward in time. Specifically, a measurement advected forward by six months (and therefore experiencing six months less melt) is balanced by a measurement advected backward by six months (experiencing six months more melt). By taking the me-

dian value within each bin, these opposing effects largely cancel each other out, resulting in a robust representation of elevation
135 (Figures 1b and c).

2.2 Basal Melt Calculations

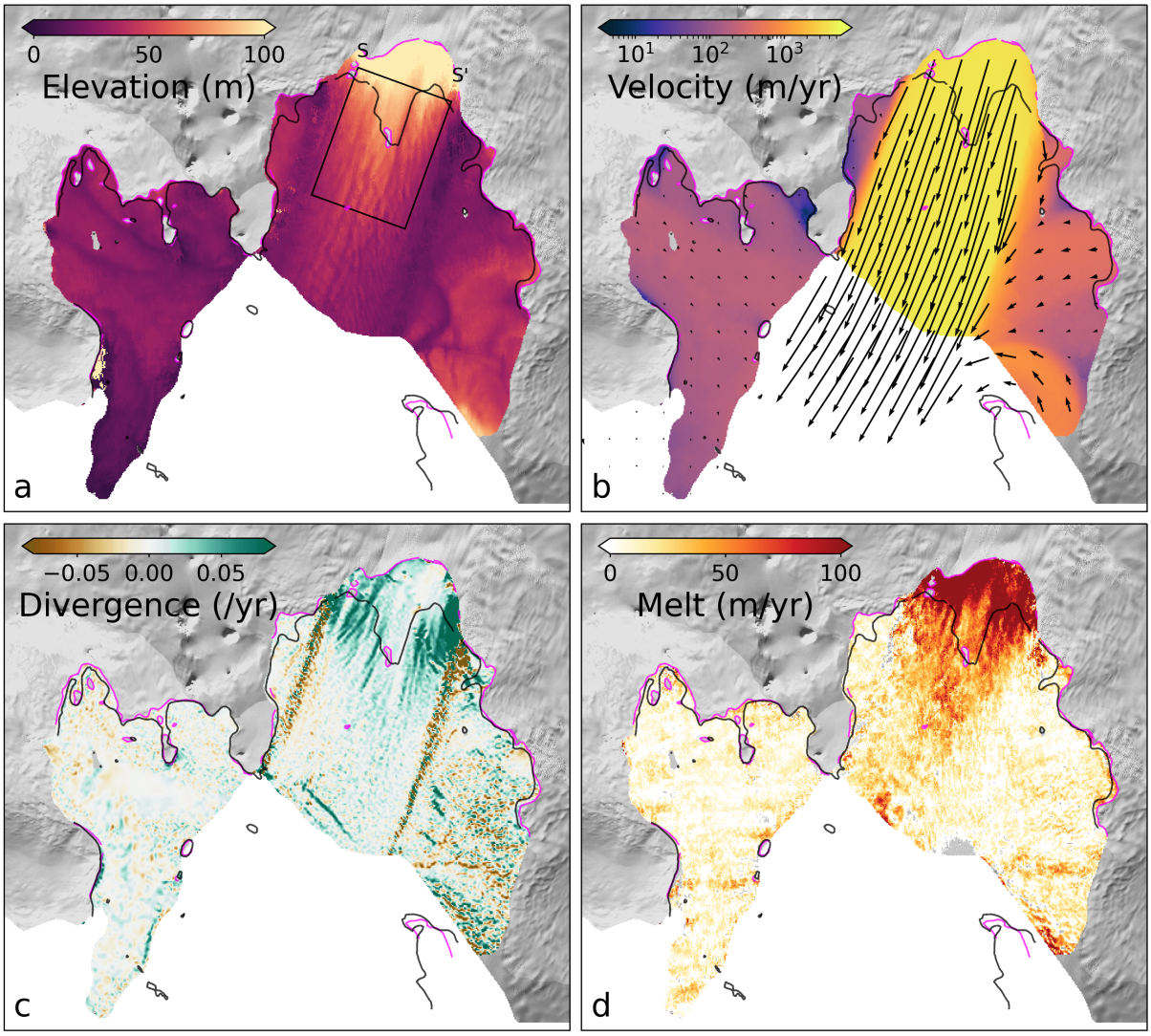

Figure 2. ~~Example basal melt calculation components.~~ (a) Digital Elevation Model derived from CryoSat-2, (b) velocity, coloured by velocity magnitude and overlaid with velocity vectors, (c) velocity divergence, and (d) basal melt rates. All components shown are in 2015. The black rectangle in (a) is for Figures 5 and 6. ~~Basemap~~ The basemap and grounding lines are as in Figure 1.

Once monthly DEMs are generated, we utilise them (e.g. Figure 2a) to calculate Lagrangian basal melt rates (Figure 2d) by employing a similar method to those detailed previously (Shean et al., 2019; Dutrieux et al., 2013; Zinck et al., 2023; Moholdt

et al., 2014; Gourmelen et al., 2017). The Lagrangian framework measures thickness change of a parcel of ice as it moves, thereby avoiding ~~Eulerian problems~~ issues associated with the advection of ~~ice~~ topographic features through the grid that arise within an Eulerian framework. Assuming floatation of the ice, basal melt rates, m, are given by:

$$m = -\frac{DH}{Dt} - H(\nabla \cdot \mathbf{u}) + s, \tag{2}$$

where

$$H = h\left(\frac{\rho_w}{\rho_w - \rho_i}\right) \tag{3}$$

is the ice thickness, $\frac{DH}{Dt}$ is the Lagrangian thickness change, $\mathbf{u}$ is the horizontal ice velocity vector, $H(\nabla \cdot \mathbf{u})$ is the thickness change resulting from flow divergence and s is the Surface Mass Balance (SMB), positive for accumulation. SMB has been taken from RACMO model outputs (Noël et al., 2018). By assuming hydrostatic equilibrium and constant ocean and ice densities, $\rho_w = 1028$ kg/m^3 and $\rho_i = 917$ kg/m^3 respectively, ice elevation, h, is converted into ice thickness, H, following equation (3). Within the ice flux divergence term, $H(\nabla \cdot \mathbf{u})$, of equation 2, H is taken from the initial DEM.

For each month, we conduct the same advection process as described in Section 2.1 to predict the location of an ice parcel after a year. Subsequently, the Lagrangian thickness change is determined by comparing the ice thickness at the original location with the thickness at its location a year later. This process yields a Lagrangian change in thickness $\left(\frac{DH}{Dt}\right)$ map that is temporally centered between the two DEMs, at the 'mid-time' stamp half a year after the start date. The Lagrangian thickness change is allocated to its original location in space, following the 'initial pixel' method outlined by Shean et al. (2019). The change in ice thickness as a result of velocity divergence ($H(\nabla \cdot \mathbf{u})$, Figure 2 c) is considered based on the original location of the ice parcel ~~and~~ at the mid-time stamp and is again calculated using the annual ITS_LIVE velocity mosaics (Figure 2b).

~~Our melt maps at monthly postings remain relatively noisy~~ Throughout the method we use an annual velocity dataset. Over our observational period PIG accelerates and the flow bends west-ward (Figure A2) following the large calving events in 2018. Therefore using a time averaged velocity field would not be appropriate. However, using annual velocity datasets introduces discrete jumps at annual boundaries. Furthermore, the annual velocity datasets are relatively noisy and this likely contributes to some noise in our melt maps. During the advection process (both for time-centring and melt advection), the velocity dataset corresponding to the year of each time step is used. Similarly, the divergence field for the melt calculation is taken from the year of the target month. We decided against interpolating between velocity datasets to avoid smoothing the channel-scale features we aim to preserve within the velocity and divergence fields (Figure 6d). The aliasing of channel-scale features when interpolating between these fields would become more prominent when channels are not aligned along flow. Our choice ensures consistency throughout the method by aligning the treatment of velocity and divergence fields.

The velocity divergence, $\nabla \cdot \mathbf{u}$, is calculated over a 480 m (two times the resolution of the velocity dataset) length scale using a centered calculation. For a given grid cell, divergence is calculated by the velocity gradient between its neighbouring cells. The output is therefore spatially centred on the initial grid cell of interest. This scale is relatively small with respect to the channel width, so we expect to capture the channelised signal of divergence without smoothing the signal within a channel.

However, it is likely that signals at the channel ~~scale~~edge are somewhat smoothed as the calculation computes gradients between points on either side of the channel boundary.

At the channel scale, our monthly posted melt maps remain relatively noisy. To further reduce the noise and obtain a coherent channelised melt signal, we further averaged 12 months of melt maps. To complete this averaging, we have advected the 12 months of melt data to their location at the middle time step using the same advection process as during time-centring, as described in Section 2.1. The advected data ~~is~~ are then re-binned, and the median melt value in the bin is taken. This averaging has been completed on a rolling 12 months basis and therefore we retain monthly posting between July 2012 and December 2021. ~~Therefore, Cryosat-2~~ Between the time-centring associated with the creation of the DEMs and that associated with noise reduction of the melt maps, elevation data spanning 3 years ~~has~~ have contributed to each monthly posted melt map.

~~We use annual velocity datasets throughout our method, which introduces discrete jumps at annual boundaries. During the advection process (both for time-centering and melt advection) the velocity dataset corresponding to the year of each time step is used. Similarly, the divergence field for the melt calculation is taken from the year of the target month. This approach avoids averaging the divergence field, which would smooth the channel-scale features we aim to preserve. This choice ensures consistency throughout the method by aligning the treatment of velocity and divergence fields~~The averaging of annual melt maps was complete within a Lagrangian framework to avoid smoothing channelised melt anomalies that are not aligned with flow. While ocean conditions set the amount of heat in the cavity, the melting caused depends on the ability of ocean circulation to bring the heat to the ice-ocean interface. These currents depends on ice shelf geometry on both large scales and channel scales. Therefore, ice movement changes the spatial distribution of melt and a Eulerian averaging would smooth over these changes.

Obtaining basal melt rates with this approach is based on several key assumptions. Specifically, it assumes that the ice is fully floating and in hydrostatic equilibrium, that the ice velocity is vertically uniform (and therefore the surface velocity is a good representation of the ice velocity at the base), and that the ice is a viscous continuum (does not fracture in response to divergence) (Dutrieux et al., 2013; Zinck et al., 2023). Bridging stresses within the ice make deriving changes within small channels through changes in surface elevation challenging (Dutrieux et al., 2013). It is important to acknowledge these limitations inherent to methods using remote sensing techniques to derive ice shelf basal melt rates, particularly when attempting to infer changes to features of similar scales to a few ice thicknesses. ~~In-situ surveys demonstrate~~ Furthermore, in-situ surveys have demonstrated the complexity of the basal geometry associated with smoother surface expressions (Dow et al., 2024; Dutrieux et al., 2014b; Drews, 2015).

2.3 Sentinel-1 Differential Range Offset Tracking

To investigate the relationship between channels and pinning points, we derive the locations of pinning point groundings using the differential range offset tracking (DROT) method applied to Sentinel-1 synthetic aperture radar (SAR) data. The DROT technique makes use of SAR sensors' off-nadir viewing geometry to detect floating ice, because vertical tidal displacements are projected into the satellite's line-of-sight and appear as an anomalous horizontal ground-range displacement in intensity feature tracking results (Joughin et al., 2016; Friedl et al., 2020; Marsh et al., 2013). By differencing adjacent feature tracking

results, or subtracting a reference steady-state ground-range velocity field, the anomalous ground-range displacement caused by vertical tidal displacement is isolated, in a process analogous to differential interferometric SAR (DInSAR). From this tidal displacement result, the grounding line and any pinning points can be delineated. Because DROT uses intensity feature tracking, rather than InSAR, to measure ice motion, it does not require InSAR coherence and is suitable for investigating pinning points on fast flowing ice shelves, such as PIG, where coherence is not routinely maintained in the 6-day repeat period of Sentinel-1.

In this study, we use 6 and 12 day repeat Sentinel-1 intensity feature tracking pairs over the PIG shelf processed using the GAMMA remote sensing software package (Strozzi et al., 2002). Tracking results are post-processed using a moving mean filter over a 1x1 km window, where values 30% greater than the mean are rejected and isolated pixels which represent poor tracking results are also removed according to a locally determined threshold (Lemos et al., 2018; Selley et al., 2021). Outputs are posted at a resolution of 100x100 m in Antarctic Polar Stereographic projection (EPSG:3031). To produce observation of ephemeral grounding and pinning points we select equitation pairs with differential tide heights greater than 0.5 m and remove the steady-state ground range velocity field by subtracting the median ground range velocity from a 180 day window centred on the measurement date to calculate the tidal motion anomaly. This anomaly is manually delineated with GIS software to determine the location of any grounded portions of the ice shelf for the selected acquisition pair.

3 Results

3.1 Channel and pinning point history

~~Figure 3 shows the annual elevation anomaly with respect to the first DEM in our time series (July 2011). Over the~~ Over the 2011-2023 observed period, the ~~ice shelf gradually thinned, and the~~ PIG calving front retreated ~~. On average~~ (Joughin et al., 2021) and the ice shelf thinned by an average of 60 m~~between 2011 and 2023 (Figure 3l), the~~ , equivalent to a mass loss of 259 Gt ~~.~~ through thinning alone (Figure 3). In addition to overall thinning, geometric features such as basal channels have evolved, imprinting small-scale features on ~~top of~~ the overall thinning ~~rates~~ pattern (Figure 3). ~~The~~

A pinning point in the centre of the ice shelf began to unground in 2011 (Joughin et al., 2016), resulting in a thick column of ice being advected downstream. This is visible ~~as~~ in the anomalously thick (red) region in the centre of Figure 3a. Over time, the entire downstream section of the ice shelf thickened as the thicker ice was transported further downstream ~~.~~ (Figure 3). The thick ice ephemerally reground as it advected downstream (Joughin et al., 2016)

~~Before~~ In 2011, a large basal channel extended downstream of the pinning point, as shown in Figure 4a (beyond ~~8km~~8 km) and in the centre of Figure 4d. We ~~hypothesise~~ hypothesis that this channel formed due to interactions between the ice and bed at the pinning point, which imprinted on the ice geometry ~~,~~and was further enhanced by concentrated melting ~~within~~ with the channel. After the pinning point ungrounded, this basal channel was gradually advected downstream and replaced by thicker ice. Therefore, the thickening trend shown in Figure 3 is as much a signal of the absence of a channel as it s a thickening with respect to the whole ice shelf. Simultaneously, a new arrangement of basal channels began forming further upstream (Figures 3 and 4).

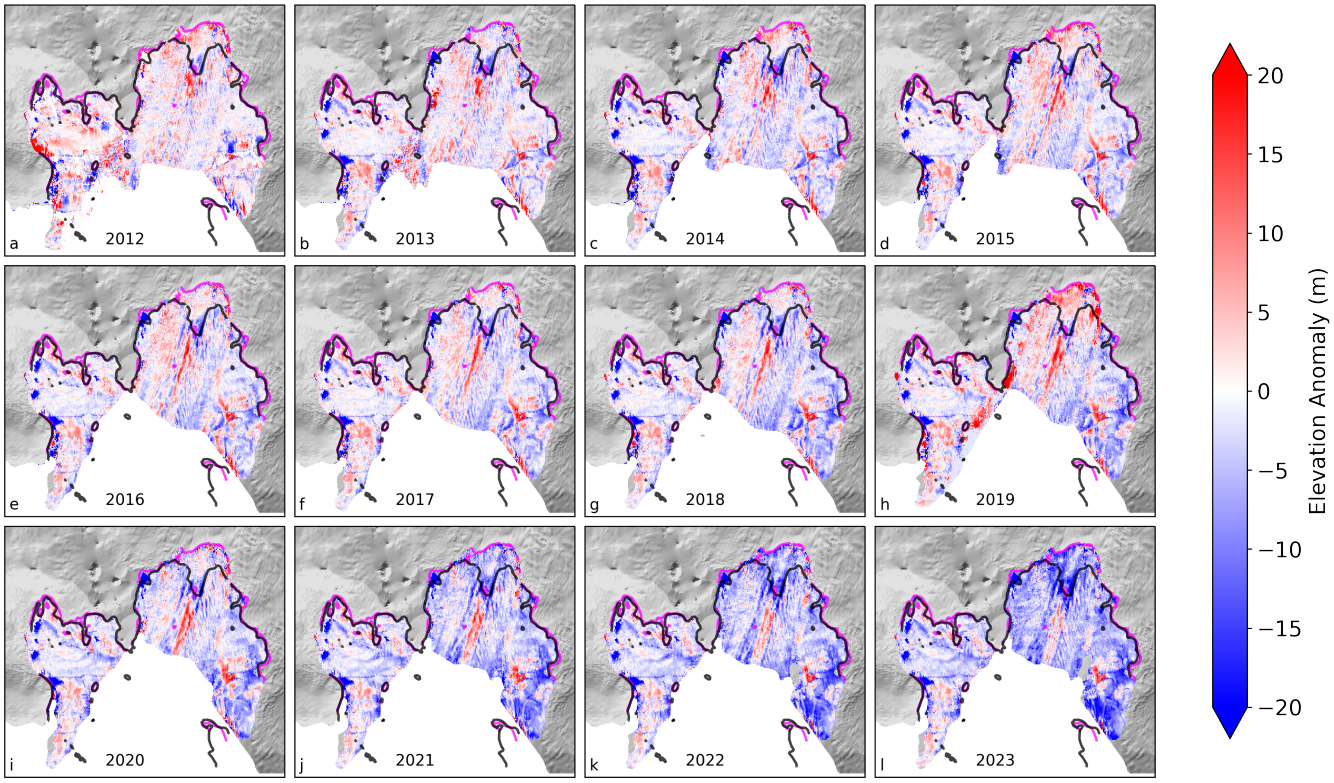

Figure 3. (a)-(l) show the annual elevation anomalies with respect to the first DEM in June 2011 for 2012-2023, respectively. Basemap and grounding lines as in Figure 1.

To investigate the relationship between basal channel distribution and grounding, we will focus on the change in the ice base depth over our observational period across 3 transects (Figure ~~4~~4). The depth of the ice shelf base has been calculated by inverting the surface elevation and assuming floatation~~.~~:

$$d = -h(\frac{\rho_i}{\rho_w - \rho_i}). \quad (4)$$

Across all 3 transects, the depth of the ice shelf in 2011 (~~light blue~~cyan), 2017 (blue) and 2023 (dark blue) have been plotted. These years represent when the pinning point was starting to unground (2011), when the pinning point ephemerally regrounded in the centre of the ice shelf (2017), and the end of our observation period (2023), when the DROT method detects no further grounding and the longer term impact of the unpinning on the distribution of basal channels can be assessed. The transect in Figure 4a is along flow (shown between X and X~~'~~' in Figure 4b) and intersects areas where the pinning point was observed to be grounded in both 2011 and 2017. The transects in Figure ~~4c~~ 4c is across flow (shown between Y and Y~~'~~' in Figure 4b) and intersects where the pinning point was until 2011. The third transect in Figure 4d is shown between Z and Z~~'~~ in Figure 4~~d is~~

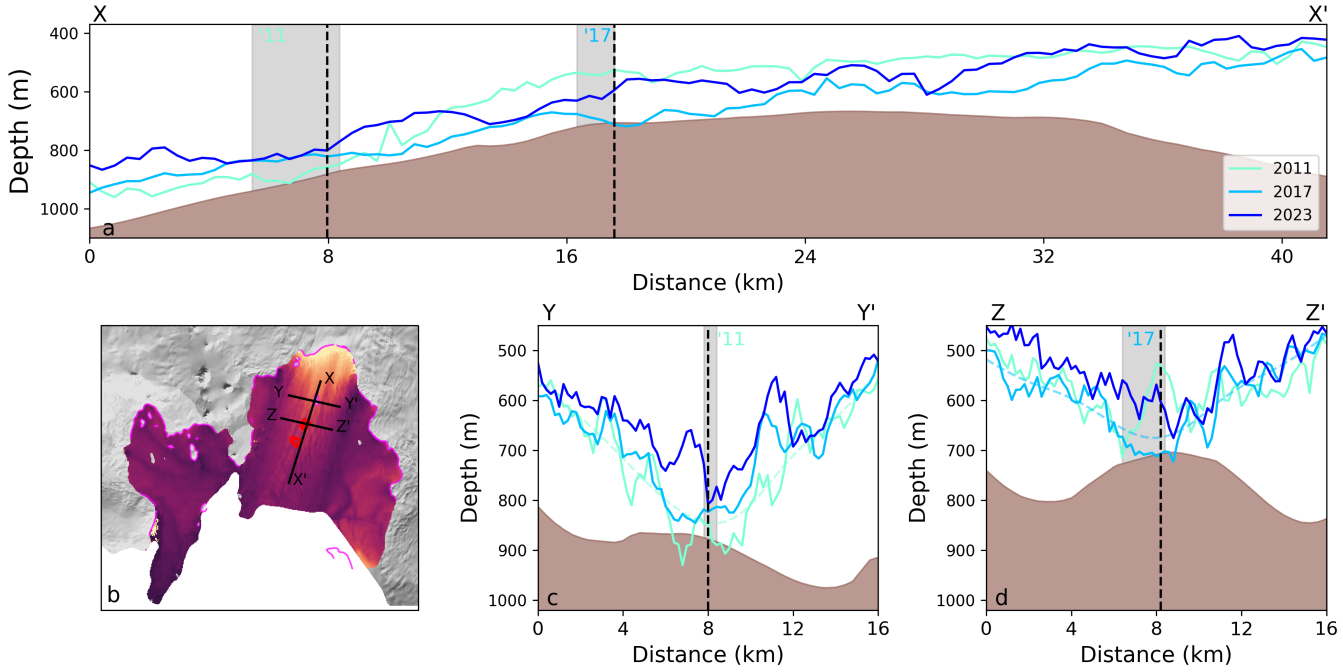

Figure 4. Depth of the ice shelf base in 2011, 2017 and 2021 across three different transects. (b) shows the three transects used in the other subplots. (a) shows the depth of the base between X and X', (c) shows the depth of the base between Y and Y', and (d) shows the depth of the base between Z and Z'. The red lines in (b) show the areas where Sentinel-1 DROT data indicates grounded ice in 2017. The vertical grey shaded areas in (a),(c) and (d) show grounded areas in 2011 and 2017 as observed by the MEaSUREs 2011 grounding line and DROT 2017. The black dashed vertical lines mark the points of intersection between transects. The brown shaded areas on (a), (c), and (d) are the seabed from BedMachine merged with observations from (Dutrieux et al., 2014b).

~~also across flow~~ b and intersects the location where Sentinel-1 observes the ice shelf to be ephemerally grounded in 2017. All 3 of these plots also show the depth of the seabed from BedMachine after merging with data collected in ~~(Dutrieux et al., 2014b)~~ Dutrieux et al. (2014b) along their respective transects. Grey vertically shaded areas show areas along the transects where the ice was grounded according to MEaSUREs grounding lines in 2011 and Sentinel-1 in 2017. ~~A dashed line is~~ Dashed lines are also plotted in ~~Figure~~ Figures 4c and d. These correspond to the depth of the smoothed ice base in 2011 and 2017, respectively~~, and represent the ice base if channels did not exist~~.

Despite the overall ice-shelf thinning during this period (Figure 3), the ice base depth along the along-flow transect doesn~~'~~'t exhibit a straightforward uniform thinning rate (Figure 4a). Downstream of the 2011 pinning point location (the shaded grey region, approximately 6-8 km along the transect), the ice shelf base is shallowest in 2011 and deepest in 2017. The 2011 depth represents the apex of the downstream channel discussed earlier (and is also visible in the 2011 base depth shown in Figure ~~4d~~4d). By 2017, this section of the ice-shelf thickens significantly as the thick column of ice is advected downstream, filling in

the basal channel. By 2023, however, the entire ice-shelf has thinned, and no part of this transect remains in contact with the seabed.

The two across-flow transects (Figures ~~4c~~ 4c and d) reveal a more predictable relationship between time and thinning. Overall, the ice shelf base becomes progressively shallower over the observational period. This is with the exception of the basal channel visible in the 2011 ice shelf base in Figure ~~4d~~4d. The contrast between this channel in the centre of the transect in 2011 and the grounding of the ice in 2017 illustrates how the thick column of ice was advected down from the initial pinning point location and changed the geometry of the ice shelf.

Figures 4c and d also demonstrate how basal channels ~~contribute~~ contributed to the persistence of the pinning point and the intermittent regrounding of the subsequent thick ice column. In both Figures a hypothetical smoothed version of the ice shelf base is shown. This ice base represents what we might expect if channels and channelised melt didn't exist and hence if all ice shelf melt were uniformly distributed across the ice shelf. In both instances the ice shelf would not have ~~grounded~~re-grounded, instead they would have left a 30-meter deep cavity between the ice shelf base and the seabed. This suggests that without a pronounced channel and keel geometry on the ice shelf base, the pinning point might not have been sustained for as long, and the thick ice may not have periodically re-grounded.

~~In Figure 4,~~ Unsurprisingly, some discrepancies exist between the grounded area predicted by Sentinel-1 DROT methods and the locations inferred by comparing CS2 ice base data with the modified BedMachine seabed depth data. Several factors contribute to this difference. The base depth calculated by inverting the elevation is calculated by assuming the ice shelf is in hydrostatic equilibrium, which we know doesn't hold near grounded regions. Further, the CS2 DEMs — and consequently the ice draft ~~—~~ - are calculated by averaging data points over a full year, which may smooth some of the finer details. Channelised structures are also under-represented on the ice surface due to bridging stresses (Wearing et al., 2021; Drews, 2015) ~~or kilometre scale~~ and kilometre-scale gradients in ice density (mainly firn air content) (Dutrieux et al., 2013), so our derived ice shelf base depth may not capture the full channel geometry. Despite these limitations, our observations align reasonably well with those from Sentinel-1.

3.2 Channelised Melt

We next use these data to assess the spatial distribution of ice shelf ~~melting at a channelised~~ melt at a channel scale. To do this, we ~~start by focusing~~ focus on the area shown by the black rectangle in Figure 2a. Figure 5 shows the thickness, Lagrangian thickness change and melt centered on July 2015 and ice flux divergence in 2015. ~~The final three variables, those that are rates, are shown as ice loss, where a positive ice loss represents thinning and a negative ice loss represents thickening of the ice shelf. At this location in 2015, the magnitude of ice loss caused by melt is highly dependent on the distance from the grounding line, whereas the ice loss from ice flux divergence doesn't appear to depend on the distance from the grounding line. The magnitude of ice loss contribution from basal melt is also significantly greater than the contribution from ice flux divergence~~ Basal melt is the largest contributor to ice thickness loss here (> 100 m/yr compared with ~ 40 m/yr ~~, respectively~~from ice-flux divergence).

In the area shown, basal channels are clearly present within the thickness map (Figure 5a, marked by the cyan and magenta arrows). However ~~, it is harder to visually separate the channelised pattern within the~~ they cannot be seen in the thickness change

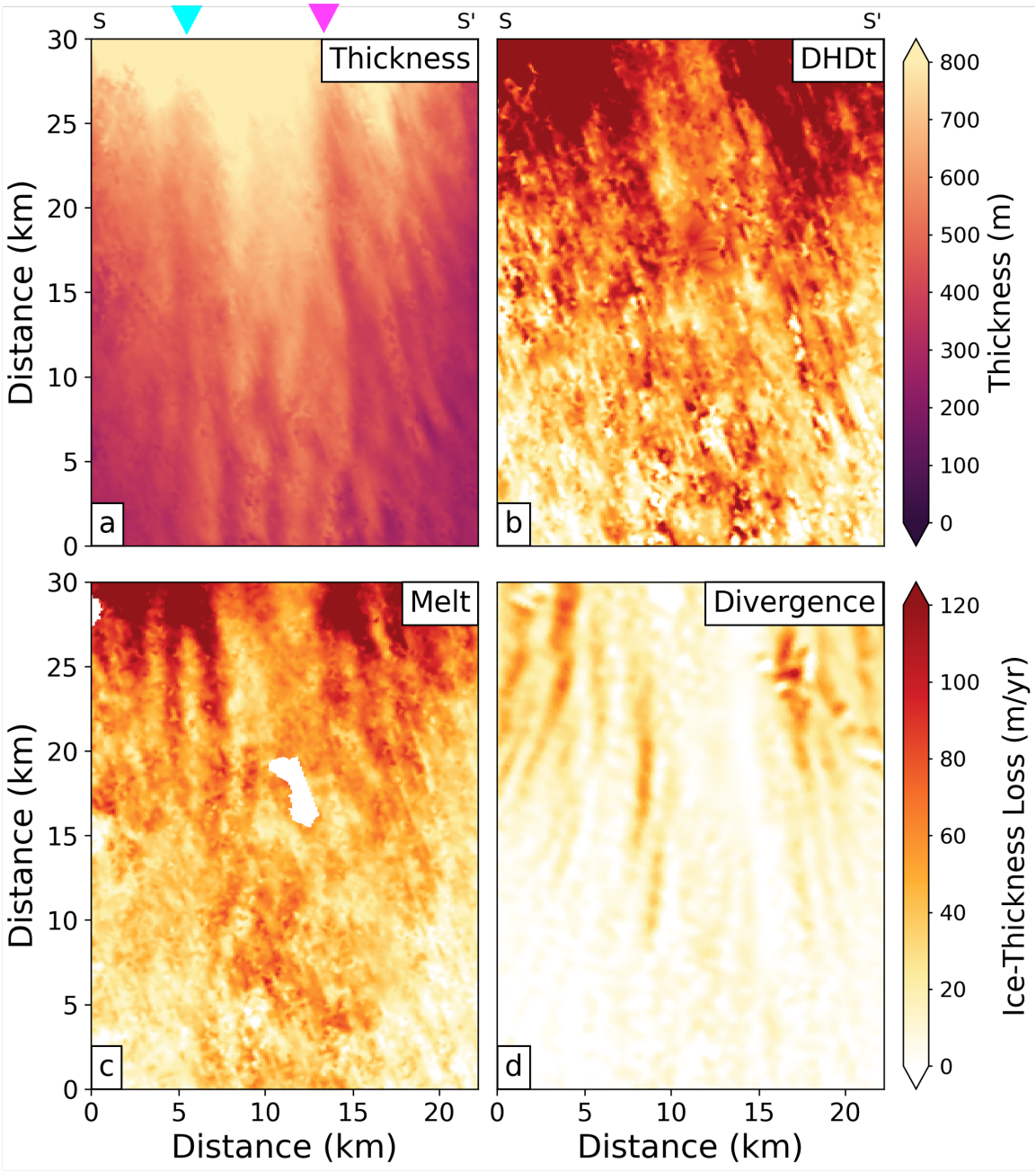

Figure 5. ~~The main variables needed to calculate basal melt rates in the black rectangle in fig 2a.~~ Thickness (a)~~Thickness~~, ~~(b)~~ Lagrangian ~~change in~~ thickness ~~,~~ changes (~~e~~b), basal melt ~~and~~ (~~d~~c) and ice flux divergence (d) in the black rectangle in Figure 2a. All variables are from 2015.

variables (Figures 5b-d). This isn't necessarily surprising, it simply suggests that in this location the change in Lagrangian thickness and flux divergence is similar inside and out of the channel. To investigate the channelised pattern ~~within these variables~~ of ice loss we will now focus on ~~high-pass-filtered~~ the high-pass filtered anomalies of these fields (Figure 6), which have been calculated by subtracting ~~low-pass-filtered fields (where each grid point is replaced by~~ a 2-D Gaussian ~~average over~~ low-pass filter with a radius of 7 km~~)~~, similarly to ~~Dutrieux et al. (2013). Figure 6 shows the same variables as in Figure 5 but as high-pass anomalies. A~~ Dutrieux et al. (2013) and Shean et al. (2019). In Figure 6 a positive ice loss anomaly means more thinning and a negative ice loss anomaly shows ~~anomalous thickening.~~ less thinning. Therefore, if the focus is on a channel, a negative anomaly indicates the channel amplitude is decreasing and a positive anomaly indicates the channel amplitude is increasing.

There are two main channels within this area that can be seen by the negative (blue) thickness anomaly in Figure 6a. They both extend the entire length of the area with little across-flow deviation. The channel ~~on the southern side of this area,~~ indicated by the ~~pink arrow ,~~ magenta arrow will be referred to as Channel 1 and the channel ~~on the northern side,~~ indicated by the cyan arrow ~~,~~ will be referred to as Channel 2 from now on. Both Channel 1 and 2 are approximately ~~2.5~~ 2 km in width but Channel 1 has an amplitude of 160 m, whereas Channel 2 has an amplitude of only 80 m. Channelised melting can be detected in both of these channels near the grounding line and particularly on the channel's ~~south~~ western flanks, where anomalies ~~are <-30~~ exceed 30 m/yr. The channelised melt pattern becomes less prominent downstream. There is also a group of smaller channels on the southern side (bottom right) of this area which are more variable in distribution ~~. Our method doesn't~~ but our method does not detect a channelised melt ~~signal~~ distribution within these smaller channels.

Figure 6d displays the ice flux divergence anomaly overlaid with velocity anomaly vectors, illustrating the influence of basal channels on both ice flux divergence and velocity. Ice flow converges into basal channels and diverges away from basal keels. This pattern can be seen right down to the smaller channels on the ~~western~~ southern side of the area, where channels are just 1 km wide with amplitudes of less than 50 m. This channel-scale distribution of secondary ice flow is consistent with a viscous response to ice thickness gradients (Wearing et al., 2021).

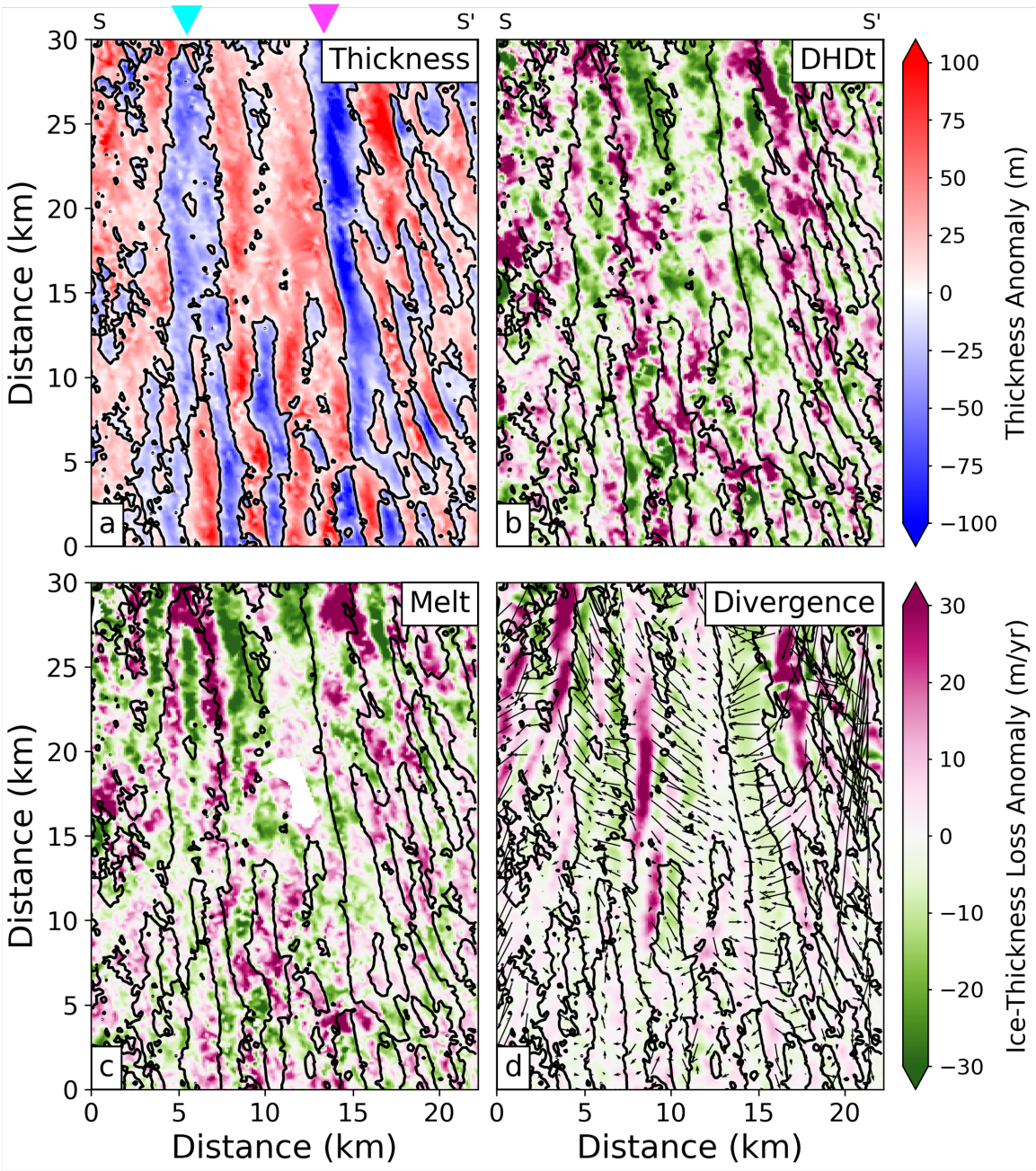

Figure 6. High-pass filtered anomaly of ~~the main variables needed to calculate basal melt rates in the black rectangle in Figure 2a.~~ thickness (a)~~Thickness anomaly~~, ~~(b)~~ Lagrangian ~~change in~~ thickness ~~anomaly,~~ change (c), basal melt ~~anomaly and~~ (~~d~~c) and ice flux divergence and velocity ~~anomalies. The black lines on all plots are~~ (d) within the ~~zero thickness anomaly contour lines~~black rectangle in figure 2a. All variables are from 2015. The pink and cyan arrows indicate Channels 1 and 2, respectively, as discussed in the text.

3.3 Channelised Melt Evolution

Although previous studies have used DEMs with a higher spatial resolution to derive melt rates (Shean et al., 2019; Zinck et al., 2023), these are less frequently acquired. The strength of CS2 data resides in its long term stability and the frequency of its sampling. With an annual moving window averaging technique, we can observe how channelised features evolve at sub-annual time-scales. Figure 7 shows the elevation (~~b,f,~~ja,e,i) and melt (~~d,h,l~~c,g,k) anomalies along different sections of the ice shelf ~~and how they change in time~~during our observing period. As in Figure 6, small-scale high-pass filtered anomalies are taken with respect to a Gaussian 2D filter with a radius of 7 km. The Gaussian filter and therefore the high-pass anomalies are re-calculated at every time step. The ~~first~~ right-hand column of Figure 7 shows the time averaged elevation (yellow in ~~a,c,e,g,i,k~~b,d,f,h,j,l) and melt (pink in ~~c,g,k~~d,h,l) anomalies across the different sections.

Figures 7b and d show the elevation and melt ~~anomaly~~anomalies, respectively, across a transect near the grounding line (solid white transect between A and A~~'~~' on Figure 1~~). This is in a~~ a where the ice shelf geometry has not been directly affected by the ungrounding of the pinning point. These panels show the transect in an Eulerian framework, so the transect location is static in time. ~~The location of this transect is between the main grounding line and the location of the pinning point in 2011. Therefore geometric changes of the ice shelf here have not been directly impacted by the change in pinning point geometry during this period .~~

During this period Channels 1 and 2 ~~remain stable throughout the entire period, retaining consistent geometries~~ have a consistent geometry (Figure 7~~b) . Both channels~~ a) and are associated with positive melt anomalies ~~along their apex~~ of 30 m/yr and 20 m/yr, respectively, along their apexes (minima in surface elevation anomaly correspond to maxima in melt anomaly~~,~~ ~~Figures 7c and d) . The time averaged melt anomalies within Channel 1 and 2 are ~ 30 m/yr and 20 m/yr and the two highest melt regions correspond to the two lowest elevation regions~~) (Figure 7c ~~).~~ and d).

~~Elevation and melt anomaly evolution for different sections on the ice shelf. (b) and (d) are the elevation and melt anomalies between A and A' in Figure 1. (f) and (h) are the elevation and melt anomalies between B and B' in Figure 1. (j) and (l) are the elevation and melt anomalies originating from A and A' in Figure 1 in a Lagrangian framework. The transect has been advected forward in time until it is between a and a' at the end of 2020. (b), (d) and (f) are overlaid with the zero contour line from (a), (c) and (e), respectively, in black. The left column of panels shows the time averaged value of elevation and melt from the adjacent panel. The pink and cyan arrows indicate Channels 1 and 2, respectively, as discussed in the text.~~

~~Figure 7f and h~~ Figure 7e and g present the elevation and melt anomalies, respectively, ~~along a transect further downstream on the ice shelf~~ across a downstream transect (solid white line between B and B~~'~~' in Figure 1~~). Similar to Figures~~ a). As in 7b and d, ~~this~~ the transect is fixed in time ~~. This transect lies about 10~~ in an Eulerian framework. The transect is about 10 km downstream of the 2011 pinning point location and therefore the elevation and melt rates across it are directly influenced by the changes in pinning point geometry. ~~At the start of the observation period, the channelised geometry is complex and evolves rapidly~~ Contrasting the transect near the grounding line, the geometry here is rapidly evolving during the start of the observed period. However, ~~by~~ following 2015 a persistent channel ~~begins forming~~ forms in the south of the transect ~~, corresponding~~ which corresponds to the upstream location of Channel 1. ~~This stabilised geometry likely reflects the impact~~ The stabilised

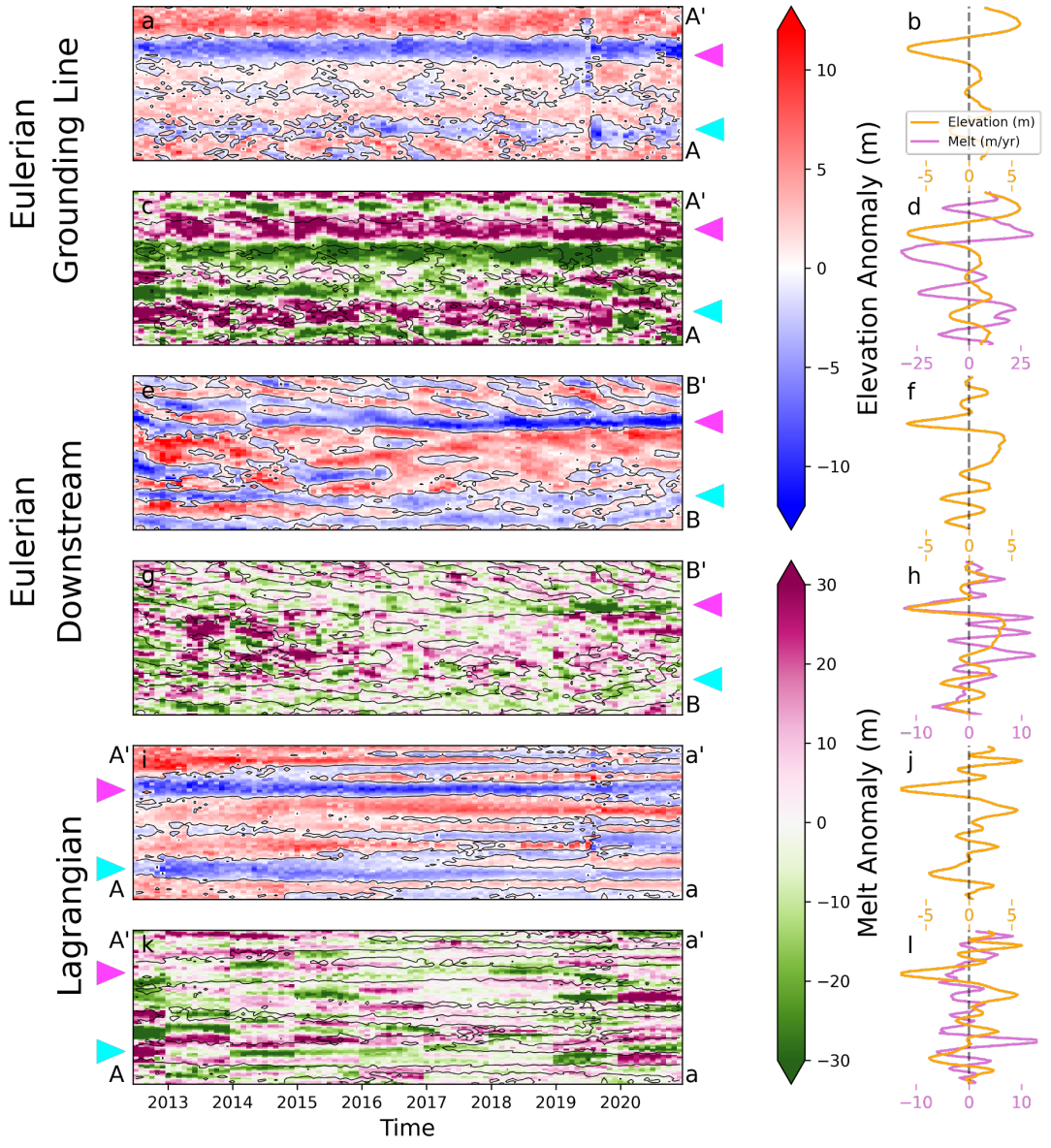

Figure 7. Elevation and melt anomaly evolution for different sections on the ice shelf. (a) and (c) are the elevation and melt anomalies between A and A' in Figure 1. (e) and (f) are the elevation and melt anomalies between B and B' in Figure 1. (i) and (k) are the elevation and melt anomalies originating from A and A' in Figure 1 in a Lagrangian framework. This transect has been advected forward in time until it is between a and a' at the end of 2020. (c), (g) and (k) are overlaid with the zero contour line from (a), (e) and (i), respectively, in black. The right hand column of panels shows the time averaged value of elevation and melt from the adjacent panel. The pink and cyan arrows indicate Channels 1 and 2, respectively, as discussed in the text.

geometry is likely a reflection of the pinning point ~~ungrounding, creating~~ ice advecting past the transect and hence a seamless connection between the ~~main~~ grounding line and ~~this location.~~

~~Within the~~ the transect has opened. Within this channel, a sustained negative melt anomaly emerges after 2016. Despite the channel~~'~~'s consistent geometry only occurring ~~from~~ in 2015, the time-averaged melt anomaly in this area remains strongly negative ~~, and the surface elevation and melt anomaly are now in phase~~ (Figure 7h). ~~This contrasts with the transect closer to the grounding line (Figures 7c and d), highlighting~~

This contrast in channel melt anomalies between near the grounding line and further downstream highlights a regime shift between the near-grounding ~~zone, where Channel 1 is~~ line, where channels are carved, and a few kilometers downstream, where ~~it is eroded. This transition aligns with a theoretical understanding where plume dynamics are more influential~~ the channel's amplitude decreases through greater melting of its keels. This is consistent with our understanding that plume dynamics have the biggest control on melt rates near the grounding line~~(see above)~~, but the depth-dependent freezing point and vertical ocean temperature distribution become more relevant downstream ~~(Dutrieux et al., 2013; Gladish et al., 2012)~~ (Gladish et al., 2012; Dutrieux et al., 2013).

~~We also note that the Coriolis offset in the melt anomaly present near the grounding line is no longer present downstream (Figures 7d and h). This could be a result of the thinner nature of the channels downstream (Millgate et al., 2013) but is more likely due to the aforementioned change in melt regime. Downstream, the keels are melting more than the channels, and therefore melt is not driven by Coriolis-influenced plume dynamics (Gladish et al., 2012).~~

~~Figures 7j and 7l~~ Figures 7i and 7k offer a Lagrangian perspective, tracking the evolution of the A-A~~'~~' transect from Figures 7~~b and d~~ a and 7c as it moves downstream on the ice shelf through to 2021. This method allows us to follow the transformation of a single cross-section of ice over time. By late ~~2020~~2021, the transect has reached the dashed white line between points a and a′ in Figure ~~1.~~ 1.

Initially spanning 2 km in width, Channel 1 persists throughout the observational period but undergoes geometric changes. Smaller channels, approximately 1–1.5 km wide, branch ~~from the central , narrow~~ off the central feature. While the primary orientations of Channels 1 and 2 remain relatively stable, these smaller branches appear to veer westward~~. This branching could result from preferential melting, carving out new channels from the keels of the parent channels (Gladish et al., 2012). It may stem from the weakening of the overall plume-driving buoyancy force beneath the ice shelf caused by the flatter background ice base slope downstream — perhaps~~ , similar to the ~~way a river delta spreads out on flatter terrain. Finally, the balance determining channel scales, an interaction between ocean and ice dynamics, could be influenced by the thinner ice towards the calving front and reduced viscous ice response to melting via secondary flows (Wearing et al., 2021).~~

~~Regardless of the mechanism driving this branching, it leads to a near doubling of the channel~~ observations from Bindschadler et al. (2011 . This process nearly doubles the channel wavenumber (the number of channels per unit distance) as the transect ~~advects downstream . Gladish et al. (2012) and Millgate et al. (2013) demonstrated that an increase in the number of channels (i.e., wavenumber)near the grounding line is associated with a reduction in overall melt rates. Despite the aforementioned presence of other factors increasing melt at the grounding line, it is interesting to note the correspondence between melt decrease and increased number of channels as the transect progresses down the ice shelf.~~ moves downstream (Figure 7i).

~~Temporal variability in this~~ The melt signal within the Lagrangian framework appears noisy and ~~is largely influenced by the spatio-temporal fluctuations in the velocity divergence field. We are currently limited to using annual velocity fields to estimate divergence. This and potentially other methodological limitations make assessing channelised melt evolution in this framework challenging. However, by comparing the channelised melt pattern in Figures 7c and 7g, it is clear that Channel 1 undergoes a noteable transition. Its apex shifts from being associated with a positive melt anomaly (indicating channel calving) to a negative melt anomaly (where the keels melt faster). Despite this regime change, the time-averaged melt anomaly within the channel remains negative (Figure 7k).~~

~~Outside Channel 1, the overall pattern of wide channels splitting into smaller branches persists. However, the melt signal exhibits noisy,~~ exhibits discontinuous steps at yearly boundaries ~~due to~~ (Figure 7k), due to the changes in the divergence field used in the melt ~~calculations~~calculation. While smaller discontinuations are visible in the melt product of the two Eulerian transects, the combination of changing space and time in the Lagrangian framework emphasises the impact of these discrete steps in the divergence ~~field. This highlights the sensitivity of melt evolution assessments to the choice of velocity divergence field.~~ fields.

3.4 Coriolis Favoured Melting

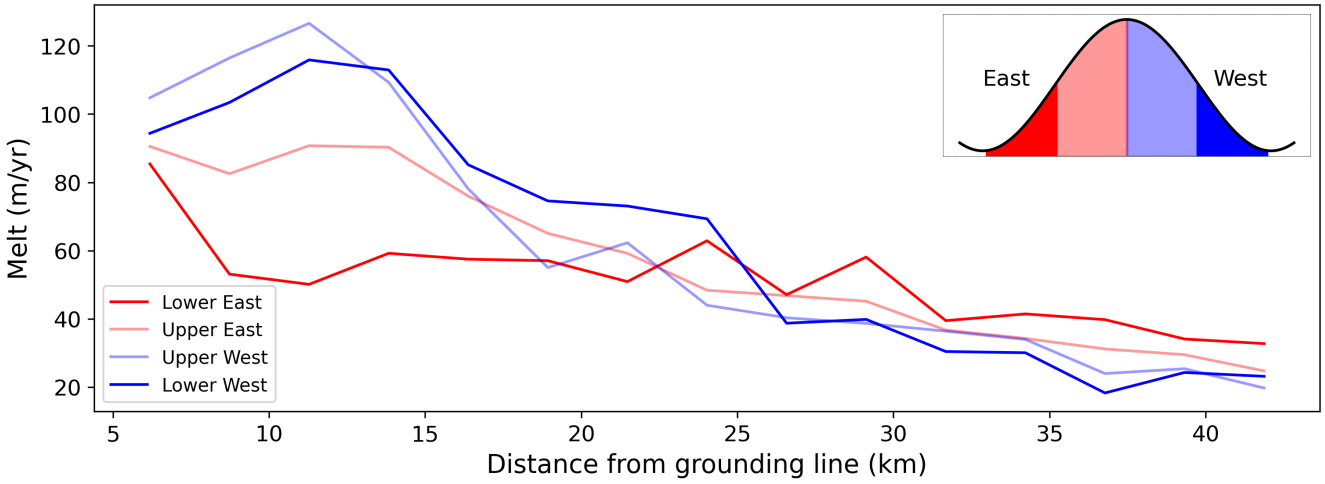

Figure 8. Comparison of ~~variables between the east and west flank~~ melt rates on different sections of Channel 1 as a function of distance from the 2011 grounding line. ~~(a) shows the depth of the channel crest and the depth of the seabed from BedMachine merged with Dutrieux et al. (2014b) observations, (b) shows the average depth of the channel crest and the east and west keel, and (c) shows the average melting on the east and west flank of the channel.~~

Several studies have hypothesised and sporadically observed that melting in channels is enhanced on the Coriolis-favoured side, particularly near the grounding line (Gladish et al., 2012; Millgate et al., 2013; Dutrieux et al., 2013; Gourmelen et al., 2017; Marsh et al., 2016; Cheng et al., 2024). To further investigate the asymmetric distribution of melting across a channel

(Figure 7c and 7d) and how this distribution varies as a function of distance from the grounding line, we now consider Channel 1 in more detail. This channel has been chosen because it is persistent in time, by the end of the observing period it extends to the calving front (Figure 7~~f~~e) and we also derive the largest melt signal within it. Therefore, we have the best chance of observing melt variations across it~~within our data~~.

~~To perform this analysis we need to compare observations on the north eastern and south western flanks of the channel at different distances from the~~

To investigate the across-channel variations in melt rates, we take across-channel transects $\sim$ every 2 km in the along flow direction, starting 6 km from the 2011 grounding line. ~~For each distance from the grounding line, an across-channel transectis drawn and the elevation and melt observations along that transect are used. To divide the melt observations into two flanks, we must first define the boundaries for these areas. The two flanks are defined as the area of ice base between the east and west keels and the channel crest, where these three points are located by extracting the turning points of the elevation anomaly across the transect (where $\frac{dh}{dx} = 0$ and $\frac{d^2h}{dx^2} \neq 0$). The location of the channel crest is then defined~~ Across each transverse transect, the channel apex and keels on either side are identified as the minimum ~~turning point and the location of the two keels are the maximum turning points~~ and maximum small scale elevation anomalies on either side~~. The location of the flank boundaries are recalculated for each month of observations to account for the changing geometry~~ , respectively. The eastern and western flanks thereby identified are further split in two equidistant subsections, effectively dividing the entire transect in 4 subsections from the eastern flank to the western flank of the channel ~~. Once the areas of the channel flanks along the transect have been defined, all melt observations on either flank are extracted. Once this method has been applied to all months in our observing period, the data is~~ (inset in Figure 8). The boundaries of these subsections are re-calculated for each transect every month. Melt rates calculated every month in each subsection are then averaged in time~~. This method is then repeated over the entire set of transects, located at different distances~~ , providing us with a time average view of the melt distribution across the persistent Channel 1, from the grounding ~~line~~zone to the calving front.

~~To classify the geometry across the transect as a channel , certain criteria are required from the observations. The~~ The algorithm contains some criteria which the data must meet to be included in our analysis. Firstly, the depth of the channel apex must be shallower than that of the keels. Secondly, the identified channel must be at least 1.5 km in width (3 grid points on either flank for a symmetric channel) ~~. If the algorithm fails to define one of the flanks , or if one flank is over~~ and the length of each of its flanks must be within 1 km ~~in width longer than the other, then all observations in that month along that transect are discarded. This has been done for two reasons: first , to remove observations where~~ of each other. These criteria first ensure the algorithm has ~~failed to correctly identify~~ correctly identified a channel, and ~~second, to ensure there isn't a significant discrepancy in~~ ensure there is not a significant difference between the number of observations ~~between channel~~ on either channel flank. This means the selected channels are symmetric enough that a comparison can be made between either flanks. ~~These criteria have been implemented to ensure the algorithm only selects data where the channel is big enough and symmetric enough to compare the melt rates on either flank of the channel. Closest~~ Close to the grounding line there are over ~~800 melt observations on either flank of the channel but further downstream there are between 200 and 400. This is because~~

at the start of the time period the channel does not extend to the end of the ice shelf, and the algorithm correctly detects no channel.

Figure 8a shows the main geometry of the ice shelf cavity beneath the channel. The ice shelf is plotted in light blue and the base depth is the channel crest depth, the seabed is brown and its depth is taken from the BedMachine merged with Dutrieux et al. (2014b) observations, and the ocean cavity between them is plotted in dark blue. All subplots here are shown as a function of the distance from the grounding line. In Figure 8b we show the average depth of the channel crest (same as 8a) and those of its east and west keels that have been extracted from the method described above. These are the three locations that act as the boundaries for 400 melt observations within each of the channel flanks. The depths of these 3 locations are calculated for every month of observations and the mean of those observations has been shown here. Figure 8c shows the mean melt on the north-eastern and south-western flanks of the channel. As with the depths, melt observations are extracted for every month of observationsand the mean of those observations has been plotted. The standard deviation of the two groups is also shown. 4 subsections of the channel, whereas downstream there are $\sim$ 100 observations.

Near the grounding line, the depths of the two channel keels are very similar melt is highest on the upper western flank followed by the lower western flank (Figure 8b). However, moving downstream, the south western flank thins more rapidly than the north eastern flank. By 20 km from the grounding line, the south western flank has almost disappeared, and the channel evolves into a more cliff-like structure. Figure 8c shows the average melt rates on either flank of the channel as a function of distance from the grounding line. Within the first 15 km from the grounding line (approximately 25% of the ice shelf), melt rates on the south western flank are over 50% higher (40–50). Averaged between the eastern and western flanks, the melt on the western flank is over 50% (40-50 m/yr) than those on the north eastern flank higher than on the eastern flank within the first 15 km of the grounding line. This asymmetry is likely driven by the Coriolis force acting on the an ocean plume within the channel , which enhances which favours the erosion of the south western flank. Similar structural evolution of channels has been observed in model results (Cheng et al., 2024). While previous studies have noted this Coriolis-driven phenomenon (Marsh et al., 2016; Dutrieux et al., 2013; Gourmelen et al., 2017) and it has been modelled extensively (Gladish et al., 2012; Millgate et al., 2013; Cheng et al., 2024), we believe this is the first clear observational quantification of the effectwestern keel (Figure 9). Higher melting on the upper half of either flank also gives evidence that the melt distribution across the channel here is dominated by a buoyant plume within the channel. 25 km or about half-way downstream from the grounding zone, the pattern reverses and melt rates on the lower eastern keel are highest (having dropped by only 40% from the near grounding zone amplitude).

3.5 Channel Formation

To predict how channel geometry — and consequently channelised melting — might evolve in the future, it is essential to understand how channels form. While various mechanisms of channel formation across Antarctica have been observed and modelled suggested by observations and modeled numerically (Le Brocq et al., 2013; Gourmelen et al., 2017; Marsh et al., 2016; Alley et al., 2016; Sergienko, 2013; Gladish et al., 2012; Millgate et al., 2013), the formation process on PIG remains uncertain. The persistence of Channel 1 throughout the CryoSat-2 CS2 observational period (Figure 7b) provide a) provides

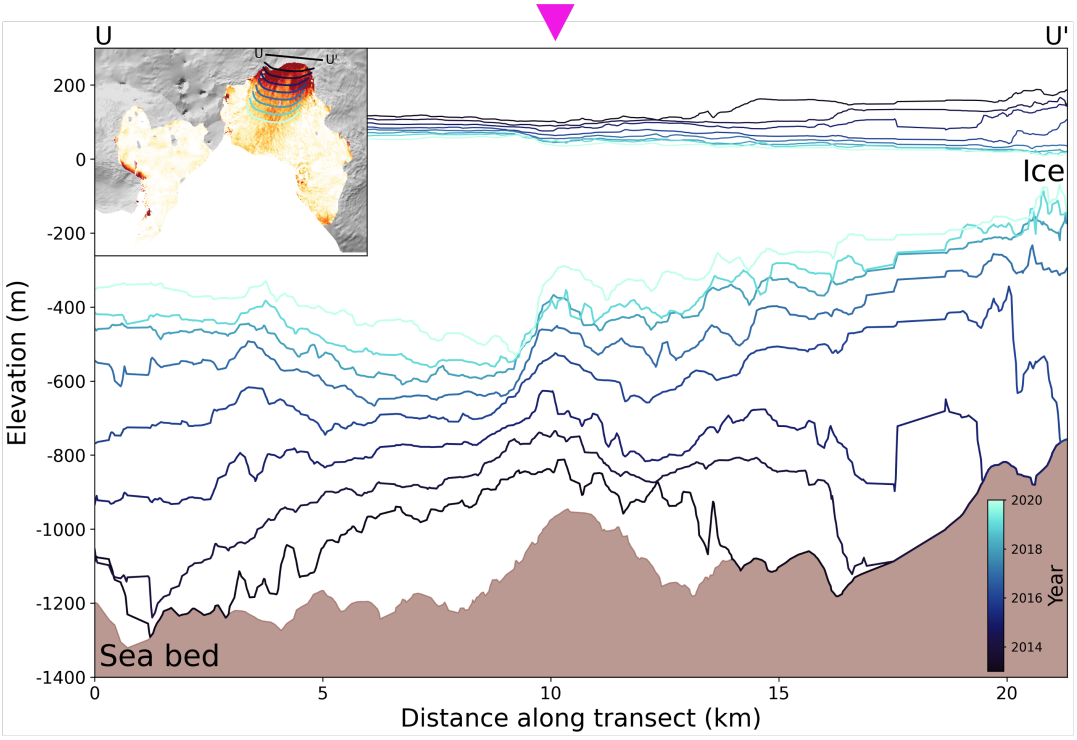

Figure 9. The brown area is the ice bed upstream of the grounding line along the black transect on the inset map, as measured from airborne radar (Vaughan et al., 2012). Using ITS_LIVE annual velocity data, the location of this flight line has been advected downstream, with the annual location of these advected transects shown on the inset map. The surface elevation and ice base depth derived from ~~CS2~~ CryoSat-2 along each of these transects has then been plotted.

new insights. This observation suggest a constant ~~formation mechanism~~ mechanism of formation that is closely linked to the grounding zone.

Figure 9 shows the seabed depth (brown) upstream of the grounding line (between U and U' on the inset map), as measured by airborne radar during the British Antarctic Survey campaign in 2004/05 (Vaughan et al., 2012). Starting in 2011, we advect the location of this flight line downstream with an annual time step. The surface elevation and depth of the ice shelf base as inferred from floatation ~~are then plotted~~ along the advected flight lines are then plotted. We have only included transects where we are confident the ice at Channel 1 is in hydrostatic equilibrium (greater than 2 ice shelf thicknesses away from the grounding line)~~.~~, hence the first year shown is 2013.

In the centre of the grounded flight line, there is a $\sim$ 200m high feature on the seabed surrounded by smaller ($\sim$ 50m high) oscillations. We note that a major part of the ice base evolution is connected to divergence from the shear margins and the associated thinning there, creating a convex glacier tongue with a thicker central line~~near the calving front~~. The channelised geometry overlays and co-evolves with these large-scale changes. Channel 1 in the centre of the ice shelf appears to inherit its shape from the large central feature in the seabed. The channel ~~, initially impacted by the presence of the pinning point~~

downstream, begins symmetric (as a reflection of the relatively symmetric bed feature) and gradually evolves to a more cliff-like topography in 2020 as a result of Coriolis-favoured melting, as discussed above (section 3.4 , Section 3.4 and Figure 8). These results suggest that channel geometry is in part a function of upstream seabed geometry on PIG and explains the persistent nature of Channel 1's geometry near the grounding line.

4 Discussion

Various approaches have been employed to calculate ice shelf melting using satellite observations (Dutrieux et al., 2013; Gourmelen et al., 2017; Zinck et al., 2023; Shean et al., 2019). In this study, we present the first time series of basal melt rates at a sub-kilometre spatial resolution, revealing the time-dependant nature of channelised geometries. On PIG ice shelf, channelised geometries exhibit variability on annual timescales (Figure 3), and both ice velocity and velocity divergence vary on spatial length scales consistent with channel structures (Figure 6d). Relying on a time-averaged dataset risks aliasing these dynamic features, potentially overlooking spatial variations in melt that contribute to the ice shelf integrated melt rate. Although this impact is especially pronounced on PIG, where abundant basal channels and rapid flow , rapid flow and recent acceleration and re-direction of ice flow (Figure A2) complicate the dynamics, we expect similar considerations to be relevant across other ice shelves. Further investigation is needed to understand the implications of these methodological choices and to determine how they vary among different ice shelves. Ultimately, the method we propose may help refine historical mass loss estimates through better estimating the spatio-temporal variations of melting on sub-kilometre scales.

Furthermore, this methodological sensitivity may affect comparisons between satellite-derived melt rates and in situ observations. Precise consideration of the spatial context of in situ measurements relative to ice shelf geometry is essential. If satellite-derived melt rates alias spatio-temporal features, a meaningful comparison with in-situ data becomes challenging.

The method We acknowledge several sources of error in both our methodology and data analysis. Noise in the CryoSat-2 data exists from its poorly constrained firn penetration depth, errors inherent to the unwrapping processes and from orbit, range and angle uncertainties. The median standard deviation in a single DEM bin is 5.8 m. There are also errors within the velocity product used. Although we have not completed a formal error propagation here, we believe these uncertainties do not alter our conclusions as they are likely consistent in time. However, a full investigation into how different datasets used impact ice shelf basal melt rate estimation would be of benefit to the community.

Further errors arise from methodological assumptions. Most prominently, the method assumes the ice shelf is in hydrostatic equilibrium. We know this does not hold near the grounding line of an ice shelf. Throughout the analysis we have used to a conservative 2011 grounding line to mask the grounded ice. All basal channel analyses supporting our conclusions have been completed in areas of the ice shelf further than 2 ice thicknesses from the 2011 grounding line and therefore in an area of the ice shelf we consider to be, on the large scale, fully floating. However, hydrostatic errors also exist on a basal channel scale. Observations have shown that the depth of the ice base can be underestimated within basal channel (Dutrieux et al., 2013; Rignot et al., 2025) due to bridging stresses within the ice. It has also been shown that the largest errors in deriving melt rates from remote sensing data occur along channel walls, where bridging stresses across ice-thickness

gradients cause the ice shelf to deviate from hydrostatic equilibrium (Drews, 2015; Wearing et al., 2021). It is expected that melt is underestimated at the channel apex as a result (Wearing et al., 2021). This error is reduced as the ice relaxes as it moves away from the grounding line. This signal of relaxation is therefore aliased within our melt observations. While such errors may affect the quantitative melt rates derived, we do not expect them to influence our qualitative conclusions, for example regarding Coriolis-favoured melting, as the errors should at least initially be symmetric across the channel.

The method we have used to estimate basal melt rates at a given time stamp (Section 2) uses elevation data spanning 3 years. All steps of the method use flow-line advection to time-centre the data and account for spatio-temporal changes. This approach addresses errors induced by feature advection through each observing window, but at the cost of introducing temporal smoothing. This creates an effective along-flow smoothing kernel of 3 years (12 km if the ice shelf is flowing at 4 km/yr) but introduces no smoothing across-flow. The method therefore permits shorter wavelengths in the across-flow direction than in the along-flow direction. Despite the disregard of the directional dependence of elevation change, we argue this decision is critical to obtain channelised signals in our dataset.

Our observations show that melt rates near the grounding line are concentrated within basal channels (Figure 8). While these observations agree with many others (Dutrieux et al., 2013; Marsh et al., 2016; Stanton et al., 2013; Gourmelen et al., 2017; Humbert et al. , it also contrasts observations made on PIG ice shelf by Shean et al. (2019). There are a number of reasons why we might see these differences in our observations. Firstly, Shean et al. (2019) only noted the highest melting on channel keels within 3-4 km of the grounding line, an area where the hydrostatic assumption begins to breakdown. Further, in their study, channels were defined as any areas where the surface elevation anomaly was < -1 m (equivalent to a thickness anomaly of ~ 9 m), and keels where the elevation anomaly was > 1 m (thickness anomaly greater than ~ 9 m). It therefore likely that observations classified as a keel in Shean et al. (2019) are defined as channel flank in this study and the discrepancy arises from different labelling choices. We also note that the algorithm used in Shean et al. (2019) identifies large portions of the grounding zone to be basal keels which might also affect the results. Furthermore, their channelised melt conclusions were deduced from a single composite melt map that spanned 7 years. It is therefore likely that across-channel melt variations were smoothed and hence no conclusions were drawn regarding Coriolis favoured melting. Conversely, our conclusions derive from analysis over only 2 persistent and larger channels, and a broader, more systematic study bringing in more observations (and associated caveats about the representations of smaller scale features) may provide a more nuanced picture.

Our findings lend strong support to theories positing that channelised melt is concentrated on the Coriolis-favoured flank, where rising buoyant plumes are deflected by Earth's rotation (Gladish et al., 2012; Millgate et al., 2013; Marsh et al., 2016; Gourmelen et . Within 15 km of the grounding ~~zone~~line, we observe ~~that ocean-driven melting intensifies along the south western flank, with melt rates~~ ocean driven melting to be approximately 50% higher ~~than those on the north eastern flank. As a result of this asymmetry, we see the near-disappearance of the south western flank of the channel and the steepening and deepening of the north eastern flank . Despite this,~~ on the western flank than the eastern flank, with the highest melt rates on the upper portion of the western flank (Figure 8). Higher melt rates are also evident on the upper portion of the eastern flank relative to its lower portion. Our results are consistent with other studies positing enhanced melting on the channel apex~~does not migrate away from the flow lines (Figure 7j) when temporal variability of ice velocity is taken into account, contrary to suggestions~~

from observation (Alley et al., 2024) but aligned with previous model predictions (Gladish et al., 2012).. Notably, this pattern reverses downstream, where the eastern keel exhibits the highest melt rates. This can be explained by the deeper eastern keel being exposed to warmer (deeper) waters and at a lower pressure-dependent freezing point. Alternatively, mid-water intrusions arising from the calving front and an associated enhanced circulation could focus melt on this flank instead.

In warm cavities such as that under PIG ice shelf, theory shows that we would expect more melting in deeper channels as more vigorous melt plumes are associated with increased friction velocity (stronger currents) and warmer near-ice temperatures (Cheng et al., 2024). It has also been shown that the Coriolis force has a larger impact on distributing melting within wider channels (Gladish et al., 2012; Millgate et al., 2013). In ocean models, once the width of a channel falls below 2 Rossby radii, the Coriolis force plays a smaller role in the momentum balance and the circulation moves away from geostrophy, tending towards geostrophic overturning (Millgate et al., 2013). Our observations , though limited mainly to 2 channels, show some agreement with these theories: the deeper Channel 1 consistently shows more melt , and the wider Consistent with previous observations (Alley et al., 2024) and modelling studies (Sergienko, 2013), the asymmetry in melt rates across Channel 1 has a persistent westward leaning melt distribution, with its western keel displaying positive melt anomalies and it's eastern keel displaying negative melt anomalies (Figure 7).

Despite the agreement of our observations with theories of narrow channels being less impacted by Coriolis-favoured melting (Millgate et al., 2013), Cheng et al. (2024) showed that if one assumes a symmetric and unchanging channel geometry across the whole length of the ice shelf, Coriolis-favoured melting persists along the whole length near the grounding line leads to the westward deviation of the channel's apex from flow (Figure 9) and the widening of the channel on the western side (Figure 7i). Despite the reversal of across-channel melting downstream, we don't observe a re-centering of the channel apex. This is likely because the melt signal is much smaller downstream of the grounding line. The rate of deviation from flow likely depends on the melt amplitude, the across-channel variation in melt and the flux divergence of the iceshelf due to the ice-ocean boundary current increasing in velocity. These theories, combined with observations , suggest the distribution of melting is determined by a complex interplay between plume dynamics, channel and ice shelf wide geometry-driven ocean circulation, and the presence of other forced ocean currents (e.g. tides). Further research is needed to better understand how this asymmetry varies spatially and temporally across different channels and ice shelves . We emphasise that these are merely observations from a single channel and further observations across a number of different channels on different ice shelves are required to gain a more in-depth understanding of this relationship.

Previous studies have shown that the largest errors in deriving melt rates from remote sensing data occur along channel walls, where bridging stresses across ice-thickness gradients cause the ice shelf to deviate from hydrostatic equilibrium (Drews, 2015; Wearing et al., 2021). Bridging stresses mean that the channel is actually deeper than inferred from surface topography and it is expected that melt is underestimated at the channel apex as a result (Wearing et al., 2021). While such errors may affect the quantitative melt rates derived, we do not expect them to influence our qualitative conclusions, for example regarding Coriolis-favoured melting, as the errors should at least initially be symmetric across the channel.

The overall contribution of basal channels to ice-shelf stability remains a subject of debate (Alley et al., 2022). Our findings confirm support a link between the existence of presence of basal channels and the ability of their keels to create ephemeral

associated keels to form pinning points. ~~By focussing~~ Concentrating melt within channels ~~, deeper keels form than if the ice melted uniformly. This increases the likelihood of grounding~~promotes the formation of deeper keels compared to scenarios with spatially uniform melting, thereby increasing the likelihood of grounding. This interpretation is consistent with previous work highlighting the role of basal keels in the intermittent regrounding of pinning points (Joughin et al., 2016). By enhancing the ~~persistence of pinning points~~longevity of the central pinning point on PIG, basal channels may have indirectly ~~delayed the~~ contributed to the delayed loss of buttressing capacity ~~on PIG. This observation aligns with previous research that highlights the role of basal keels in the intermittent regrounding of pinning points (Joughin et al., 2016)~~of the ice shelf. Alternatively, transient pinning could act as a focal point for localised ice strain, potentially leading to crevassing and rifting in areas with strong thinning gradients (Arndt et al., 2018). While our results do not provide a definitive answer on this point, nor do they quantify whether pinning points form or persist due to the advection of basal channels around Antarctica, they highlight the complex role of channel-pinning point interactions in ~~ice-shelf~~ ice shelf dynamics.

~~The formation mechanism of basal channels varies significantly across Antarctic ice shelves, with key implications for ice-shelf stability and melt patterns. Notably, the primary channel on PIG retains its form from upstream of the grounding line, where bed elevation variations directly imprint onto the ice shelf base. The coupling between the bed and the ice shelf base determines the spatial distribution of basal melting, concentrating the highest melt rates within the Channel 1. These findings suggest that channel distribution is closely linked to the underlying bed geometry, and therefore, changes in grounding line position would likely shift the distribution of basal channels and basal melting. This highlights the dynamic nature of basal channels as both products and regulator of ice shelf geometry and stability.~~

5 Conclusions

This study analyses the spatial and temporal changes in channelised ice shelf melting on Pine Island Glacier between 2011 and 2023 using CryoSat-2 surface elevation data. We have demonstrated that it is possible to use these data to derive monthly DEMs and melt-maps at a 250 m spatial resolution over Antarctic ice shelves. Furthermore, we emphasise the importance of incorporating accurate velocity divergence field when calculating ice shelf basal melt rates on channel scales from satellite data. This precision is crucial for capturing small-scale spatial changes, as high spatial frequency melt and thickness gradients significantly impact small scale ice velocity divergence anomalies. These methodological conclusions have important implications for future satellite observations of ice shelf basal melt, potentially enhancing the accuracy of historical ice loss estimates.

Using the data presented here, we have shown the evolution of basal channels on PIG, emphasising their interactions with pinning point dynamics and their role in modulating basal melt rates. The main channel on PIG inherits its shape upstream of the grounding line from an ice bed hill. Once floating, ocean melt is concentrated on its Coriolis-favoured flank. Within 15 km of the grounding line, melting on the Coriolis-favoured (~~south~~ western) flank of a channel can be over 50% greater than on the ~~north~~ eastern flank. This channel, and its corresponding keel, contribute to the ~~formation~~ persistence of the central pinning point on PIG ~~. This channel geometry facilitates~~ and it's ephemeral re-grounding ~~as it moves~~ downstream, potentially influencing ice-shelf stability.

Code availability. The code used in the melt calculation can be found here: https://github.com/katiel1108/PIG_melt.

~~The code used in the melt calculation can be found here: .~~

Data availability. We are currently working with the Polar Data Centre to create a DOI for the DEMs and melt maps created and used in this study.

~~We are currently working with the Polar Data Centre to create a DOI for the DEMs and melt maps created and used in this study.~~

Appendix A

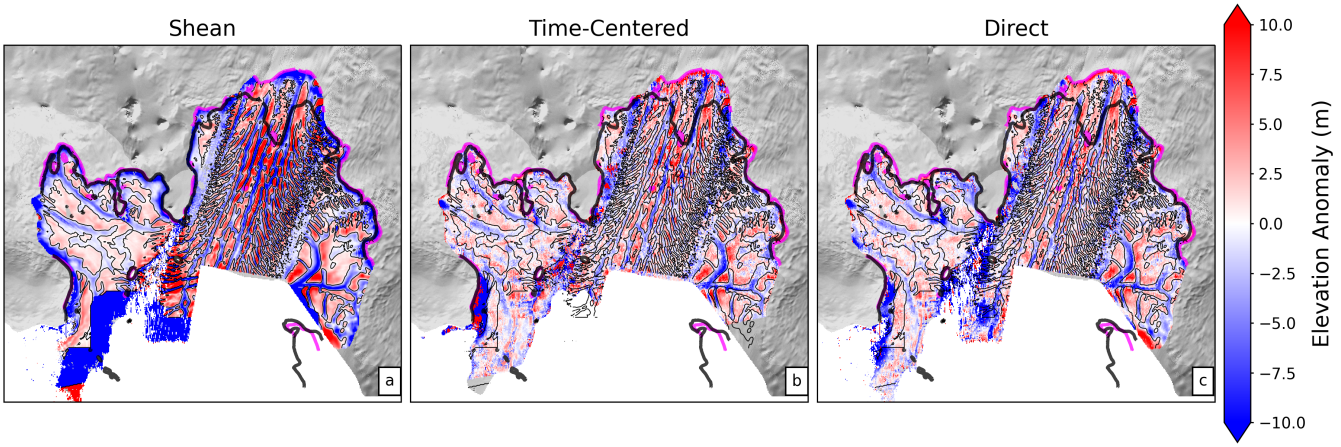

Figure A1. ~~PIG DEMs in 2015 generated by~~ High-pass elevation anomaly for (a) ~~direct binning and~~ Shean et al. (2019) DEM, (b) ~~time-centering.~~ time-centered DEM and (c) ~~is~~ direct DEM. All plots are overlaid with the ~~difference between (a) and (b)~~Shean et al. (2019) elevation anomaly zero contour lines in black.

Author contributions. KL, PD and PH planned the research; KL conducted the data analysis, except the Sentinal-1 DROT data which were processed by BJW. KL wrote the manuscript. All authors provided insights on data interpretation and reviewed and edited the manuscript.

~~KL, PD and PH planned the research; KL conducted the data analysis, except the Sentinal-1 DROT data which were processed by BJW. KL wrote the manuscript. All authors provided insights on data interpretation and reviewed and edited the manuscript.~~

Competing interests. We declare that the authors have no competing interests.

~~We declare that the authors have no competing interests.~~

Acknowledgements. This work was led by Katie Lowery at the British Antarctic Survey (BAS) and the School of Earth and Environment at the University of Leeds. Katie Lowery was supported by the Natural Environment Research Council (NERC) Satellite Data in Environmental Science (SENSE) Centre for Doctoral Training (grant no. NE/T00939X/1). This research was supported by OCEAN ICE, which is co-funded by the European Union, Horizon Europe Funding Programme for research and innovation under grant agreement Nr. 101060452 and by UK Research and Innovation. OCEAN ICE Contribution number ~~XX.~~ 19. The authors gratefully acknowledge the European Space Agency (ESA)

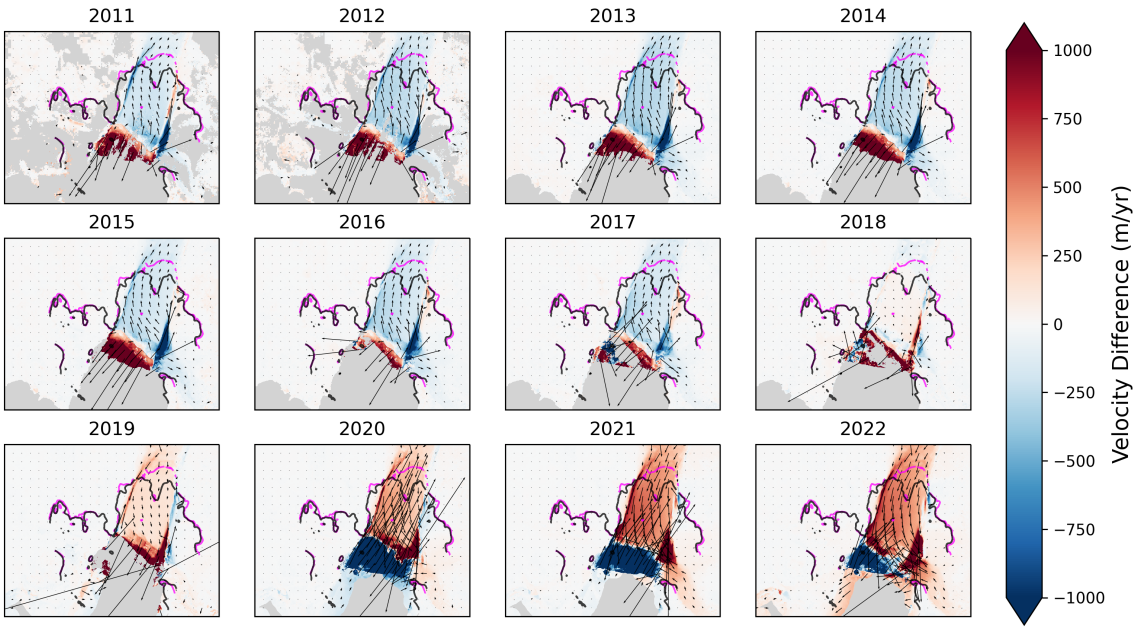

Figure A2. PIG annual velocity difference with the time averaged velocity over this period.

and the European Commission for the acquisition and availability of Copernicus Sentinel-1 data. Benjamin J. Wallis was supported by the Panorama Natural Environment Research Council (NERC) Doctoral Training Partnership (DTP), under grant NE/S007458/1, and the UK EO Climate Information Service, under grant NE/X019071/1.

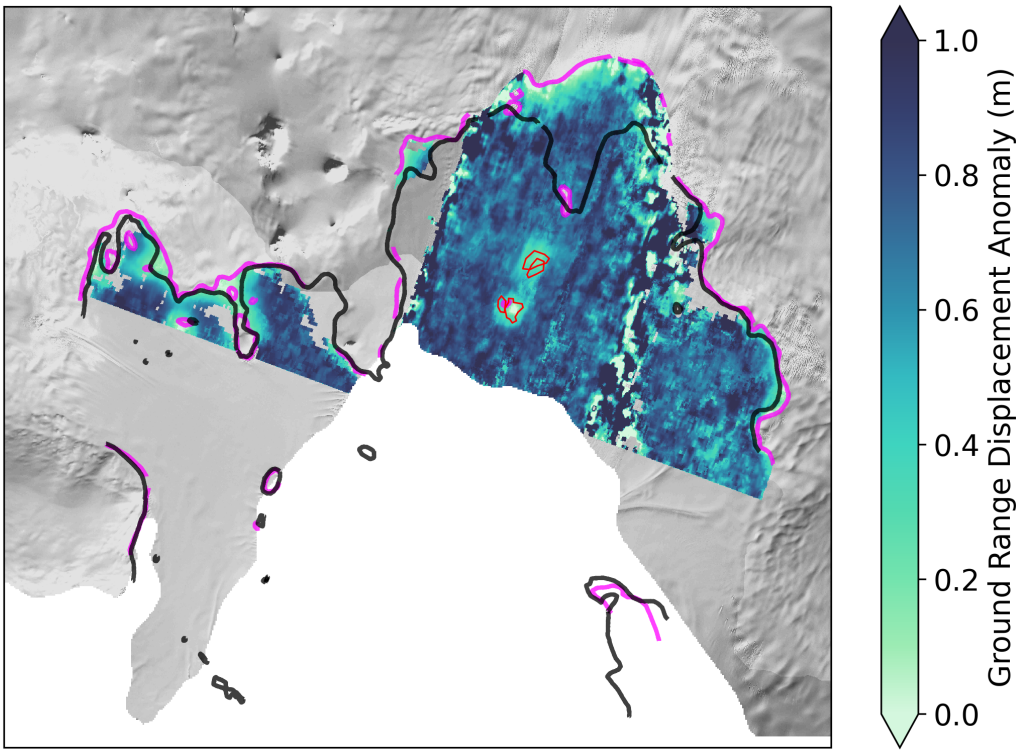

Figure A3. An example of the ground range vertical displacement anomaly as calculated by applying the DROT method to Sentinel-1 data. The red contour lines show the manually delineated areas of grounded ice. The data shown is calculated by comparing acquisitions from 2017/01/27 and 2017/02/02 with respective tide heights of 0.65 and 0.11 m.

References

Adusumilli, S., Fricker, H. A., Medley, B., Padman, L., and Siegfried, M. R.: Interannual variations in meltwater input to the Southern Ocean from Antarctic ice shelves, Nature Geosciences, 13, 616–620, https://doi.org/10.1038/s41561-020-0616-z, 2020.

Alley, K., Scambos, T., Siegfried, M., and et al.: Impacts of warm water on Antarctic ice shelf stability through basal channel formation., Nature Geosciences, 9, 290–293, https://doi.org/https://doi.org/10.1038/ngeo2675, 2016.

Alley, K. E., Scambos, T. A., and Alley, R. B.: The role of channelized basal melt in ice-shelf stability: recent progress and future priorities, Annals of Glaciology, 63, 18–22, https://doi.org/10.1017/aog.2023.5, 2022.

Alley, K. E., Alley, R. B., Crawford, A. D., Ochwat, N., Wild, C. T., Marson, J., Snow, T., Muto, A., Pettit, E. C., Child, S. F., and et al.: Evolution of sub-ice-shelf channels reveals changes in ocean-driven melt in West Antarctica, Journal of Glaciology, p. 1–15, https://doi.org/10.1017/jog.2024.20, 2024.

Arndt, J. E., Larter, R. D., Friedl, P., Gohl, K., Höppner, K., and the Science Team of Expedition PS104: Bathymetric controls on calving processes at Pine Island Glacier, The Cryosphere, 12, 2039–2050, https://doi.org/10.5194/tc-12-2039-2018, 2018.

Bett, D. T., Bradley, A. T., Williams, C. R., Holland, P. R., Arthern, R. J., and Goldberg, D. N.: Coupled ice–ocean interactions during future retreat of West Antarctic ice streams in the Amundsen Sea sector, The Cryosphere, 18, 2653–2675, https://doi.org/10.5194/tc-18-2653-2024, 2024.

Bindschadler, R., Vaughan, D. G., and Vornberger, P.: Variability of basal melt beneath the Pine Island Glacier ice shelf, West Antarctica, Journal of Glaciology, 57, 581–595, https://doi.org/10.3189/002214311797409802, 2011.

Cheng, C., Jenkins, A. A., Holland, P. R., Wang, Z., Dong, J., and Liu, C.: Ice shelf basal channel shape determines channelized ice-ocean interactions, Nature Comminications, 15, https://doi.org/https://doi.org/10.1038/s41467-024-47351-z, 2024.

Davis, P. E. D., Jenkins, A., Nicholls, K. W., Brennan, P. V., Abrahamsen, E. P., Heywood, K. J., Dutrieux, P., Cho, K.-H., and Kim, T.-W.: Variability in Basal Melting Beneath Pine Island Ice Shelf on Weekly to Monthly Timescales, Journal of Geophysical Research: Oceans, 123, 8655–8669, https://doi.org/https://doi.org/10.1029/2018JC014464, 2018.

Davis, P. E. D., Nicholls, K. W., Holland, D. M., Schmidt, B. E., Washam, P., Riverman, K. L., Arthern, R. J., Vaňková, I., Eayrs, C., Smith, J. A., Anker, P. G. D., Mullen, A. D., Dichek, D., Lawrence, J. D., Meister, M. M., Clyne, E., Basinski-Ferris, A., Rignot, E., Queste, B. Y., Boehme, L., Heywood, K. J., Anandakrishnan, S., and Makinson, K.: Suppressed basal melting in the eastern Thwaites Glacier grounding zone, Nature, 614, 479–485, https://doi.org/10.1038/s41586-022-05586-0, 2023.

Davison, B. J., Hogg, A. E., Gourmelen, N., Jakob, L., Wuite, J., Nagler, T., Greene, C. A., Andreasen, J., and Engdahl, M. E.: Annual mass budget of Antarctic ice shelves from 1997 to 2021, Science Advances, 9, eadi0186, https://doi.org/10.1126/sciadv.adi0186, 2023.

De Rydt, J. and Naughten, K.: Geometric amplification and suppression of ice-shelf basal melt in West Antarctica, The Cryosphere, 18, 1863–1888, https://doi.org/10.5194/tc-18-1863-2024, 2024.

Dow, C. F., Mueller, D., Wray, P., Friedrichs, D., Forrest, A. L., McInerney, J. B., Greenbaum, J., Blankenship, D. D., Lee, C. K., and Lee, W. S.: The complex basal morphology and ice dynamics of the Nansen Ice Shelf, East Antarctica, The Cryosphere, 18, 1105–1123, https://doi.org/10.5194/tc-18-1105-2024, 2024.

Drews, R.: Evolution of ice-shelf channels in Antarctic ice shelves, The Cryosphere, 9, 1169–1181, https://doi.org/10.5194/tc-9-1169-2015, 2015.

Drews, R., Pattyn, F., Hewitt, I., and et al.: Actively evolving subglacial conduits and eskers initiate ice shelf channels at an Antarctic grounding line., Nature Communications, 8, 2017.

Dupont, T. K. and Alley, R. B.: Assessment of the importance of ice-shelf buttressing to ice-sheet flow, Geophysical Research Letters, 32, https://doi.org/https://doi.org/10.1029/2004GL022024, 2005.

Dutrieux, P., Vaughan, D. G., Corr, H. F. J., Jenkins, A., Holland, P. R., Joughin, I., and Fleming, A. H.: Pine Island glacier ice shelf melt distributed at kilometre scales, The Cryosphere, 7, 1543–1555, https://doi.org/10.5194/tc-7-1543-2013, 2013.

Dutrieux, P., Rydt, J. D., Jenkins, A., Holland, P. R., Ha, H. K., Lee, S. H., Steig, E. J., Ding, Q., Abrahamsen, E. P., and Schröder, M.: Strong Sensitivity of Pine Island Ice-Shelf Melting to Climatic Variability, Science, 343, 174–178, https://doi.org/10.1126/science.1244341, 2014a.

Dutrieux, P., Stewart, C., Jenkins, A., Nicholls, K. W., Corr, H. F. J., Rignot, E., and Steffen, K.: Basal terraces on melting ice shelves, Geophysical Research Letters, 41, 5506–5513, https://doi.org/https://doi.org/10.1002/2014GL060618, 2014b.

Favier, L., Durand, G., Cornford, S., and et al: Retreat of Pine Island Glacier controlled by marine ice-sheet instability, Nature Climate Change, 4, 117–121, https://doi.org/10.1038/nclimate2094, 2014.

Favier, L., Pattyn, F., Berger, S., and Drews, R.: Dynamic influence of pinning points on marine ice-sheet stability: a numerical study in Dronning Maud Land, East Antarctica, The Cryosphere, 10, 2623–2635, https://doi.org/10.5194/tc-10-2623-2016, 2016.

Friedl, P., Weiser, F., Fluhrer, A., and Braun, M. H.: Remote sensing of glacier and ice sheet grounding lines: A review, Earth-Science Reviews, 201, 102 948, https://doi.org/https://doi.org/10.1016/j.earscirev.2019.102948, 2020.

Gladish, C. V., Holland, D. M., Holland, P. R., and Price, S. F.: Ice-shelf basal channels in a coupled ice/ocean model, Journal of Glaciology, 58, 1227–1244, https://doi.org/10.3189/2012JoG12J003, 2012.

Goldberg, D., Holland, D. M., and Schoof, C.: Grounding line movement and ice shelf buttressing in marine ice sheets, Journal of Geophysical Research: Earth Surface, 114, https://doi.org/https://doi.org/10.1029/2008JF001227, 2009.

Goldberg, D. N., Gourmelen, N., Kimura, S., Millan, R., and Snow, K.: How Accurately Should We Model Ice Shelf Melt Rates?, Geophysical Research Letters, 46, 189–199, https://doi.org/https://doi.org/10.1029/2018GL080383, 2019.

Gourmelen, N., Goldberg, D. N., Snow, K., Henley, S. F., Bingham, R. G., Kimura, S., Hogg, A. E., Shepherd, A., Mouginot, J., Lenaerts, J. T. M., Ligtenberg, S. R. M., and van de Berg, W. J.: Channelized Melting Drives Thinning Under a Rapidly Melting Antarctic Ice Shelf, Geophysical Research Letters, 44, 9796–9804, https://doi.org/https://doi.org/10.1002/2017GL074929, 2017.

Gourmelen, N., Escorihuela, M., Shepherd, A., Foresta, L., Muir, A., Garcia-Mondéjar, A., Roca, M., Baker, S., and Drinkwater, M.: CryoSat-2 swath interferometric altimetry for mapping ice elevation and elevation change, Advances in Space Research, 62, 1226–1242, https://doi.org/https://doi.org/10.1016/j.asr.2017.11.014, the CryoSat Satellite Altimetry Mission: Eight Years of Scientific Exploitation, 2018.

Gudmundsson, G. H.: Ice-shelf buttressing and the stability of marine ice sheets, The Cryosphere, 7, 647–655, https://doi.org/10.5194/tc-7-647-2013, 2013.

Howard, S. L., Erofeeva, S., and Padman, L.: CATS2008: Circum-Antarctic Tidal Simulation version 2008, Antarctic Program (USAP) Data Center, https://doi.org/10.15784/601235, 2019.

Humbert, A., Christmann, J., Corr, H. F. J., Helm, V., Höyns, L.-S., Hofstede, C., Müller, R., Neckel, N., Nicholls, K. W., Schultz, T., Steinhage, D., Wolovick, M., and Zeising, O.: On the evolution of an ice shelf melt channel at the base of Filchner Ice Shelf, from observations and viscoelastic modeling, The Cryosphere, 16, 4107–4139, https://doi.org/10.5194/tc-16-4107-2022, 2022.

Jacobs, S. S., Hellmer, H. H., and Jenkins, A.: Antarctic Ice Sheet melting in the southeast Pacific, Geophysical Research Letters, 23, 957–960, https://doi.org/10.1029/96GL00723, 1996.

Jenkins, A., Shoosmith, D., Dutrieux, P., Jacobs, S., Wan Kim, T., Hoon Lee, S., Kyung Ha, H., and Stammerjohn, S.: West Antarctic Ice Sheet retreat in the Amundsen Sea driven by decadal oceanic variability., Nature Geoscience, 11, 733–738, https://doi.org/https://doi.org/10.1038/s41561-018-0207-4, 2018.

Joughin, I., Rignot, E., Rosanova, C. E., Lucchitta, B. K., and Bohlander, J.: Timing of Recent Accelerations of Pine Island Glacier, Antarctica, Geophysical Research Letters, 30, https://doi.org/https://doi.org/10.1029/2003GL017609, 2003.

Joughin, I., Smith, B. E., and Holland, D. M.: Sensitivity of 21st century sea level to ocean-induced thinning of Pine Island Glacier, Antarctica, Geophysical Research Letters, 37, https://doi.org/https://doi.org/10.1029/2010GL044819, 2010.

Joughin, I., Smith, B. E., and Medley, B.: Marine Ice Sheet Collapse Potentially Under Way for the Thwaites Glacier Basin, West Antarctica, Science, 344, 735–738, https://doi.org/10.1126/science.1249055, 2014.

Joughin, I., Shean, D. E., Smith, B. E., and Dutrieux, P.: Grounding line variability and subglacial lake drainage on Pine Island Glacier, Antarctica, Geophysical Research Letters, 43, 9093–9102, https://doi.org/https://doi.org/10.1002/2016GL070259, 2016.

Joughin, I., Shapero, D., Smith, B., Dutrieux, P., and Barham, M.: Ice-shelf retreat drives recent Pine Island Glacier speedup, Science Advances, 7, eabg3080, https://doi.org/10.1126/sciadv.abg3080, 2021.

Le Brocq, A., Ross, N., Griggs, J., and et al.: Evidence from ice shelves for channelized meltwater flow beneath the Antarctic Ice Sheet., Nature Geosci, 6, 945–948, https://doi.org/10.1038/ngeo1977, 2013.

Lemos, A., Shepherd, A., McMillan, M., Hogg, A. E., Hatton, E., and Joughin, I.: Ice velocity of Jakobshavn Isbræ, Petermann Glacier, Nioghalvfjerdsfjorden, and Zachariæ Isstrøm, 2015–2017, from Sentinel 1-a/b SAR imagery, The Cryosphere, 12, 2087–2097, https://doi.org/10.5194/tc-12-2087-2018, 2018.

Marsh, O. J., Rack, W., Floricioiu, D., Golledge, N. R., and Lawson, W.: Tidally induced velocity variations of the Beardmore Glacier, Antarctica, and their representation in satellite measurements of ice velocity, The Cryosphere, 7, 1375–1384, https://doi.org/10.5194/tc-7-1375-2013, 2013.

Marsh, O. J., Fricker, H. A., Siegfried, M. R., Christianson, K., Nicholls, K. W., Corr, H. F. J., and Catania, G.: High basal melting forming a channel at the grounding line of Ross Ice Shelf, Antarctica, Geophysical Research Letters, 43, 250–255, https://doi.org/https://doi.org/10.1002/2015GL066612, 2016.

Medley, B., Joughin, I., Smith, B. E., Das, S. B., Steig, E. J., Conway, H., Gogineni, S., Lewis, C., Criscitiello, A. S., McConnell, J. R., van den Broeke, M. R., Lenaerts, J. T. M., Bromwich, D. H., Nicolas, J. P., and Leuschen, C.: Constraining the recent mass balance of Pine Island and Thwaites glaciers, West Antarctica, with airborne observations of snow accumulation, The Cryosphere, 8, 1375–1392, https://doi.org/10.5194/tc-8-1375-2014, 2014.

Millgate, T., Holland, P. R., Jenkins, A., and Johnson, H. L.: The effect of basal channels on oceanic ice-shelf melting, Journal of Geophysical Research: Oceans, 118, 6951–6964, https://doi.org/https://doi.org/10.1002/2013JC009402, 2013.

Moholdt, G., Padman, L., and Fricker, H. A.: Basal mass budget of Ross and Filchner-Ronne ice shelves, Antarctica, derived from Lagrangian analysis of ICESat altimetry, Journal of Geophysical Research: Earth Surface, 119, 2361–2380, https://doi.org/https://doi.org/10.1002/2014JF003171, 2014.

Motyka, R. J., Truffer, M., Fahnestock, M., Mortensen, J., Rysgaard, S., and Howat, I.: Submarine melting of the 1985 Jakobshavn Isbræ floating tongue and the triggering of the current retreat, Journal of Geophysical Research: Earth Surface, 116, https://doi.org/https://doi.org/10.1029/2009JF001632, 2011.

Mouginot, J., Rignot, E., and Scheuchl, B.: Sustained increase in ice discharge from the Amundsen Sea Embayment, West Antarctica, from 1973 to 2013, Geophysical Research Letters, 41, 1576–1584, https://doi.org/https://doi.org/10.1002/2013GL059069, 2014.

Naughten, K. A., Holland, P. R., and De Rydt, J.: Unavoidable future increase in West Antarctic ice-shelf melting over the twenty-first century., Nature Climate Change, 13, 1222–1228, https://doi.org/10.1038/s41558-023-01818-x, 2023.

Nicholls, K. W., Corr, H. F., Stewart, C. L., Lok, L. B., Brennan, P. V., and Vaughan, D. G.: A ground-based radar for measuring vertical strain rates and time-varying basal melt rates in ice sheets and shelves, Journal of Glaciology, 61, 1079–1087, https://doi.org/10.3189/2015JoG15J073, 2015.

Noël, B., van de Berg, W. J., van Wessem, J. M., van Meijgaard, E., van As, D., Lenaerts, J. T. M., Lhermitte, S., Kuipers Munneke, P., Smeets, C. J. P. P., van Ulft, L. H., van de Wal, R. S. W., and van den Broeke, M. R.: Modelling the climate and surface mass balance of polar ice sheets using RACMO2 – Part 1: Greenland (1958–2016), The Cryosphere, 12, 811–831, https://doi.org/10.5194/tc-12-811-2018, 2018.

Paolo, F. S., Gardner, A. S., Greene, C. A., Nilsson, J., Schodlok, M. P., Schlegel, N.-J., and Fricker, H. A.: Widespread slowdown in thinning rates of West Antarctic ice shelves, The Cryosphere, 17, 3409–3433, https://doi.org/10.5194/tc-17-3409-2023, 2022.

Recchia, L., Scagliola, M., Giudici, D., and Kuschnerus, M.: An Accurate Semianalytical Waveform Model for Mispointed SAR Interferometric Altimeters, IEEE Geoscience and Remote Sensing Letters, 14, 1537–1541, https://doi.org/10.1109/LGRS.2017.2720847, 2017.

Rignot, E., Bamber, J., van der Broeke, M., and et al.: Recent Antarctic ice mass loss from radar interferometry and regional climate modelling., Nature Geoscience, 1, 106–110, https://doi.org/10.1038/ngeo102, 2008.

Rignot, E., Jacobs, S., Mouginot, J., and Scheuchl, B.: Ice-Shelf Melting Around Antarctica, Science, 341, 266–270, https://doi.org/10.1126/science.1235798, 2013.

Rignot, E., Mouginot, J., Morlighem, M., Seroussi, H., and Scheuchl, B.: Widespread, rapid grounding line retreat of Pine Island, Thwaites, Smith, and Kohler glaciers, West Antarctica, from 1992 to 2011, Geophysical Research Letters, 41, 3502–3509, https://doi.org/https://doi.org/10.1002/2014GL060140, 2014.

Rignot, E., Mouginot, J., and Scheuchl, B.: MEaSUREs Antarctic Grounding Line from Differential Satellite Radar Interferometry, Version 2, https://doi.org/10.5067/IKBWW4RYHF1Q, 2016.

Rignot, E., Mouginot, J., Scheuchl, B., van den Broeke, M., van Wessem, M. J., and Morlighem, M.: Four decades of Antarctic Ice Sheet mass balance from 1979–2017, Proceedings of the National Academy of Sciences, 116, 1095–1103, https://doi.org/10.1073/pnas.1812883116, 2019.

Rignot, E., Chauche, N., Gadi, R., Ehrenfeucht, S., and Ciraci, E.: Grounding Line Remote Operated Vehicle (GROV) Survey of the Ice Shelf Cavity of Petermann Glacier, Greenland, Geophysical Research Letters, 52, e2024GL113 400, https://doi.org/https://doi.org/10.1029/2024GL113400, 2025.

Schlegel, N.-J., Seroussi, H., Schodlok, M. P., Larour, E. Y., Boening, C., Limonadi, D., Watkins, M. M., Morlighem, M., and van den Broeke, M. R.: Exploration of Antarctic Ice Sheet 100-year contribution to sea level rise and associated model uncertainties using the ISSM framework, The Cryosphere, 12, 3511–3534, https://doi.org/10.5194/tc-12-3511-2018, 2018.

Schmidt, B., Washam, P., Davis, P., and et al.: Heterogeneous melting near the Thwaites Glacier grounding line, Nature, 614, 471–478, https://doi.org/10.1038/s41586-022-05691-0, 2023.

Selley, H., Hogg, A., Cornford, S., Dutrieux, P., Shepherd, A., Wuite, J., Floricioliu, D., Kusk, A., Nagler, T., Gilbert, L., Slater, T., and Kim, T.: Widespread increase in dynamic imbalance in the Getz region of Antarctica from 1994 to 2018, Nature Communications, 12, https://doi.org/0.1038/s41467-021-21321-1, 2021.

Sergienko, O. V.: Basal channels on ice shelves, Journal of Geophysical Research: Earth Surface, 118, 1342–1355, https://doi.org/doi.org/10.1002/jgrf.20105, 2013.

Shean, D. E., Joughin, I. R., Dutrieux, P., Smith, B. E., and Berthier, E.: Ice shelf basal melt rates from a high-resolution digital elevation model (DEM) record for Pine Island Glacier, Antarctica, The Cryosphere, 13, 2633–2656, https://doi.org/10.5194/tc-13-2633-2019, 2019.

Shepherd, A., Wingham, D., and Rignot, E.: Warm ocean is eroding West Antarctic Ice Sheet, Geophysical Research Letters, 31, https://doi.org/10.1029/2004GL021106, 2004.

Shepherd, A., Gilbert, L., Muir, A. S., Konrad, H., McMillan, M., Slater, T., Briggs, K. H., Sundal, A. V., Hogg, A. E., and Engdahl, M. E.: Trends in Antarctic Ice Sheet Elevation and Mass, Geophysical Research Letters, 46, 8174–8183, https://doi.org/https://doi.org/10.1029/2019GL082182, 2019.

Shepherd, A. e. a.: Mass balance of the Antarctic Ice Sheet from 1992 to 2017, Nature, 558, 219–222, https://doi.org/https://doi.org/10.1038/s41586-018-0179-y, 2018.

Smith, B., Fricker, H. A., Gardner, A. S., Medley, B., Nilsson, J., Paolo, F. S., Holschuh, N., Adusumilli, S., Brunt, K., Csatho, B., Harbeck, K., Markus, T., Neumann, T., Siegfried, M. R., and Zwally, H. J.: Pervasive ice sheet mass loss reflects competing ocean and atmosphere processes, Science, 368, 1239–1242, https://doi.org/10.1126/science.aaz5845, 2020.

Stanton, T. P., Shaw, W. J., Truffer, M., Corr, H. F. J., Peters, L. E., Riverman, K. L., Bindschadler, R., Holland, D. M., and Anandakrishnan, S.: Channelized Ice Melting in the Ocean Boundary Layer Beneath Pine Island Glacier, Antarctica, Science, 341, 1236–1239, https://doi.org/10.1126/science.1239373, 2013.

Strozzi, T., Luckman, A., Murray, T., Wegmuller, U., and Werner, C.: Glacier motion estimation using SAR offset-tracking procedures, IEEE Transactions on Geoscience and Remote Sensing, 40, 2384–2391, https://doi.org/10.1109/TGRS.2002.805079, 2002.

Surawy-Stepney, T., Hogg, A. E., Cornford, S. L., and Hogg, D. C.: Mapping Antarctic crevasses and their evolution with deep learning applied to satellite radar imagery, The Cryosphere, 17, 4421–4445, https://doi.org/10.5194/tc-17-4421-2023, 2023.

Vaughan, D. G., Corr, H. F. J., Bindschadler, R. A., Dutrieux, P., Gudmundsson, G. H., Jenkins, A., Newman, T., Vornberger, P., and Wingham, D. J.: Subglacial melt channels and fracture in the floating part of Pine Island Glacier, Antarctica, Journal of Geophysical Research: Earth Surface, 117, https://doi.org/https://doi.org/10.1029/2012JF002360, 2012.

Vaňková, I., Cook, S., Winberry, J. P., Nicholls, K. W., and Galton-Fenzi, B. K.: Deriving Melt Rates at a Complex Ice Shelf Base Using In Situ Radar: Application to Totten Ice Shelf, Geophysical Research Letters, 48, e2021GL092 692, https://doi.org/https://doi.org/10.1029/2021GL092692, 2021.

Veldhuijsen, S. B. M., van de Berg, W. J., Brils, M., Kuipers Munneke, P., and van den Broeke, M. R.: Characteristics of the 1979–2020 Antarctic firn layer simulated with IMAU-FDM v1.2A, The Cryosphere, 17, 1675–1696, https://doi.org/10.5194/tc-17-1675-2023, 2023.

Wearing, M. G., Stevens, L. A., Dutrieux, P., and Kingslake, J.: Ice-Shelf Basal Melt Channels Stabilized by Secondary Flow, Geophysical Research Letters, 48, e2021GL094 872, https://doi.org/https://doi.org/10.1029/2021GL094872, 2021.

Wingham, D. J., Wallis, D. W., and Shepherd, A.: Spatial and temporal evolution of Pine Island Glacier thinning, 1995–2006, Geophysical Research Letters, 36, https://doi.org/https://doi.org/10.1029/2009GL039126, 2009.

Wuite, J., Nagler, T., Gourmelen, N., Escorihuela, M. J., Hogg, A. E., and Drinkwater, M. R.: Sub-Annual Calving Front Migration, Area Change and Calving Rates from Swath Mode CryoSat-2 Altimetry, on Filchner-Ronne Ice Shelf, Antarctica, Remote Sensing, 11, https://doi.org/10.3390/rs11232761, 2019.

Zinck, A.-S. P., Wouters, B., Lambert, E., and Lhermitte, S.: Unveiling spatial variability within the Dotson Melt Channel through high-resolution basal melt rates from the Reference Elevation Model of Antarctica, The Cryosphere, 17, 3785–3801, https://doi.org/10.5194/tc-17-3785-2023, 2023.